Chapter 12
Nanotechnology for Energy Storage

12.1 Introduction

Nanomaterials of metal oxides have been intensively studied as anode and cathode materials for lithium-ion batteries (LiBs) aimed at achieving higher specific capacities and high power density. It is worth pointing out that the word "nanotechnology" has become very popular and is used to describe many types of research where the characteristic dimensions are much less than 1 μm. For example, continued improvements in lithography to design computer components have resulted in line widths that are less than one micron: this work is often called "nanotechnology." Many of the exponentially improving trends in computer hardware capability have remained steady for the last 50 years. Today "nanosciences" are fairly widespread with the belief that these trends are likely to continue for at least several years; however, new aspects are now considered in the field of energy transformation. In this respect, the classic 1959 article "There's plenty of room at the bottom" by Richard P. Feynman discusses the limits of miniaturization and forecast the ability to ". . .arrange the atoms the way we want; the very atoms, all the way down!" [1].

Nano-structured materials are distinguished from conventional polycrystalline materials by the size of the structural entities that comprises them, microstructures comprising nanoscale domains in at least one dimension. The ability to control a material's structure and composition at the nano-level has demonstrated that materials and devices having properties intrinsically different from their polycrystalline counterparts can be fabricated. As tailoring of fundamental properties becomes possible at the atomic level, the prospect of developing novel materials and devices with new applications become viable.

Conventional rechargeable Li batteries exhibit rather poor rate performance, even compared with old technologies such as lead-acid [2]. Achieving high rate rechargeable Li-ion batteries depends ultimately of the dimension of the active particles for both negative and positive electrodes. One of the prospective solutions for the preparation of electrodes with high power density is the choice of

© Springer International Publishing Switzerland 2016

C. Julien et al., *Lithium Batteries*, DOI 10.1007/978-3-319-19108-9_12

nanocomposite materials because the geometric design of the insertion compound is a crucial intrinsic property. The performance of electrode materials for Li-ion batteries reached today is the result of intensive research to reduce the size of the particles to the nanoscale. It is important, however, to specify what "nano" means here. In electronics, for instance, it signifies particles that are so small the electronic or the magnetic properties are modified by quantum confinement of the electrons. It means particles smaller than 10 nm. In the physics and electrochemistry of the cathode elements of Li-ion batteries, however, the term is used to signify particles so small that their properties depend importantly on surface effects. Typically, the surface layer is about 3 nm thick, so that particles are labeled "nano" in the literature if their size is smaller than 100 nm, and usually in the range 20–100 nm. So far, there has been little interest to synthesize smaller particles because too small particles have been reported to reduce the tap density [3] and they are much more difficult to handle in making electrodes for the industry of Li-ion batteries. It turns out that some size effects on the physical and chemical properties of the particles have been observed in this "nano" range, as we see later in this review, but they were not necessarily expected and may not be totally understood. Still, there have been many efforts through the years to decrease the size of the particles from a few microns to this "nano" range, for several reasons. One is the increase of the effective contact area of the powder with the electrolyte. A larger effective contact surface with the electrolyte means a greater probability to drain Li^+ ions from the electrode, which increases the power density of the cell. A smaller particle size also reduces the Li diffusion length to the interior of the particle, which leads to a greater capacity at higher charge–discharge rates and therefore to a larger power density. Reducing the dimensions of the active particles to nanoscale means, for a given chemical diffusion coefficient of Li^+ ions, D^*, the characteristic time, τ, for the intercalation reaction decreases by a factor of 10^6, since the characteristic time constant for intercalation is expressed by:

$$\tau = L^2/4\pi D^*, \tag{12.1}$$

where L is the diffusion length [4]. Nanoparticles, as well as more tailored nanostructures, are being explored and exploited to enhance rate, even for materials with poor intrinsic electronic conductivity such as olivine frameworks. For such a compound, by preparing the materials at the nanoscale form and by carbon coating, high rate are achievable [5]. In addition, the small electronic conductivity of the olivine particles that results from a two-phase $FePO_4/LiFePO_4$ reaction has led to coating of the particles with a thin layer that is conductive of both electrons and Li, usually an amorphous carbon layer [6]. Decreasing the particle size reduces the length of the tunneling barrier for electrons to travel from/to the surface layer or to/from the core of the particle, which also increases the power density. The coat may also decrease the activation energy for Li^+ transfer across the electrode–electrolyte interfaces.

This chapter is organized as follows. The first part is devoted to the synthesis and physicochemical properties of nanoscale functional electrode materials in various

shapes, i.e., nanoparticles, nanofibers, nanobelts. Compounds such as LiMO_2 with M = (Ni,Co), (Ni,Mn,Co), MnO_2, $LiFePO_4$, WO_3-SiO_2 nanocomposite, WO_3 nanorods, and Li_2MnO_3 rock-salt nanoparticles are examined. Various parameters that influence electrochemical performance such as particle morphology, particle size distribution are discussed. In the second part we present a specific technique of characterization that is vibrational spectroscopy (FTIR and Raman), a powerful tool for investigating the structural properties at the local scale of nanomaterials.

12.2 Synthesis Methods of Nanomaterials

The fabrication of low-dimensional nanostructures such as nanotubes, nanorods, nanofibers, nanoneedles, and nanowires had achieved a lot of attention among the researchers due to their promising applications in many advanced systems. There are two major categories into which preparative technique of nanomaterials can be classified: the physical "top-down" approach such as milling, and the chemical "bottom-up" approach such as sol–gel wet chemistry. Note that the former physical technique receives a great deal more interest in the industrial sector [7]. As a general rule, lower temperature reactions and shorter reaction times are then possible and they yield materials of higher homogeneity and higher specific area [8].

12.2.1 Wet-Chemical Methods

Wet-chemistry, also named soft-chemistry or "chimie douce," refers to synthetic technique that implies a liquid phase. There has been a great deal of interest in preparation of polycrystalline materials, particularly oxides synthesized at low temperature ($T > 200$ °C). This method consists of acidification of aqueous solutions of the starting materials. The overall process includes several steps as shown in the schematic chart Fig. 12.1: (1) mixing of starting materials in the liquid phase, (2) formation of the gel by evaporation, (3) formation of the precursor by heating the gel at low temperature and (4) calcination procedure at different firing temperatures to obtain the final product. The wet-chemical techniques could be classified in four groups according the salts and complexing agent used (Table 12.1). They are namely sol–gel [9, 10], co-precipitation [11, 12], combustion [13], pyrolysis [14], polyol [15], Pechini process [16, 17], etc.; they were employed for the preparation of nanostructured metal oxides devoted to electrodes for Li-ion batteries. These techniques are assisted by chelating agents that are carboxylic acids like citric, oxalic, malic, tartaric, and succinic [18]. Pereira-Ramos has critically discussed the impact afforded by soft-chemistry techniques especially sol–gel synthesis and precipitation techniques on the electrochemical behavior of the oxide materials as prepared [19]. Solution preparative techniques allow a better mixing of the

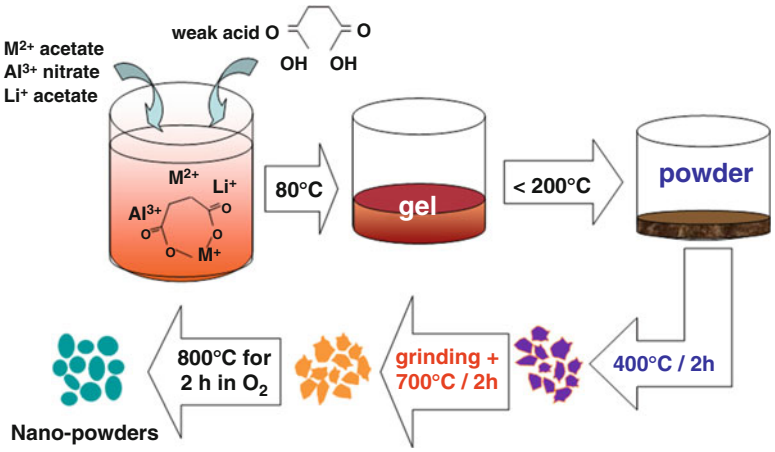

Fig. 12.1 Wet-chemical method assisted by carboxylic acid

Table 12.1 The various wet-chemistry methods used to growth transition-metal oxide powders

Method	Salts	Complexing agent	Molecular weight (g mol^{-1})	Molecular formula
Sol–gel	Acetates	Citric acid	192.43	$HOC(COOH)(CH_2COOH)_2$
Co-precipitation	Acetates	Oxalic acid	90.04	HOOCCOOH
Combustion	Nitrates	Glycine	75.07	NH_2CH_2COOH
Pyrolysis	Acetates	Succinic acid	118.09	$HOOCCH_2CH_2COOH$

elements and thus a better reactivity of the mixture to obtain purer reaction products. Lower reaction temperature and shorter reaction time are then possible to yield a compound of high homogeneity and high specific area. Moreover, these low-temperature methods make use of lower calcination temperatures resulting in particles of smaller size and a highly strained lattice.

12.2.1.1 Sol–Gel Method

The sol–gel method is based on the preparation of a colloidal suspension, a sol, and its transition to a gel from which the polycrystalline material can be obtained via inorganic polymerization reactions in solution. In the sol–gel process, a solid phase is formed through gelation of a colloidal suspension. Drying of the gel can then give "dry gel" (xerogel) state and subsequent heat treatment can be used to remove unreacted organic residues, stabilize the gel, densify it, and induce crystallinity. As an example, Fig. 12.2 shows the DTA-TG curves of the $LiNi_{0.5}Co_{0.5}O_2$ xerogel. The weak endothermic effect associated with a small weight loss of about 9 % for $T < 250$ °C are attributed to departure of residual water. A strong exothermic peak appears at 316 °C after the departure of the remaining water molecule. This

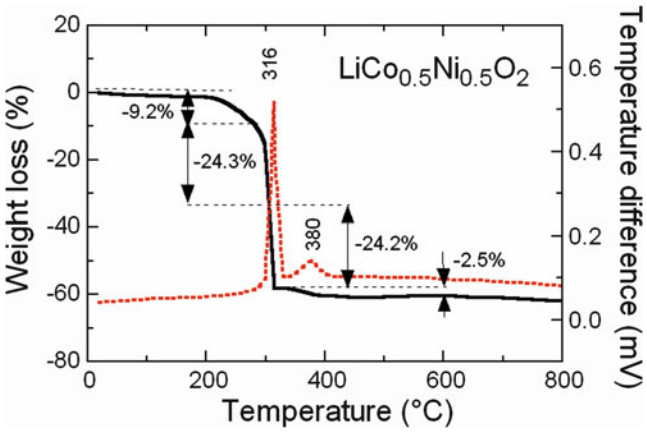

Fig. 12.2 TG-DTA curves of the $LiNi_{0.5}Co_{0.5}O_2$ xerogel. Measurements were carried out at heating rate of 10 °C per min with oxygen flow

exothermic effect corresponds to the combustion of citric acid and acetate ions xerogel. More than half of the weight loss occurs during this stage because of a violent oxidation decomposition reaction. It appeared that citric acid (formed by –COOH– groups) acts as a fuel in the pyrolysis of the gel precursor, accelerating the decomposition of acetate ions. It was reported that chelating agent (carboxylic acid) provides combustion heat for calcination in the synthesis of oxide powders [20]. The gel precursor was self-burning once ignited, because the decomposed acetate ions acted as oxidizer. The weight loss in the temperature range 330–400 °C corresponds to the decomposition of the remaining organic constituents. Even though the crystallization starts below 400 °C; thus well-crystallized and pure phases have been obtained at 600 °C. While the pyrolysis at this stage was very complicated, it could be presumed that the last weak exothermic at ca. 380 °C in the DTA curve corresponds to the crystallization of the $LiNi_{0.5}Co_{0.5}O_2$ phase [9].

12.2.1.2 Pechini Technique

In 1967, in manufacturing ceramic capacitors, Maggio Pechini developed a sol–gel technique for synthesis of alkaline-earth titanates and niobates, materials which do not have favorable hydrolysis equilibrium [21]. In the Pechini method, otherwise *polymerizable complex method*, chelating of cations is realized with the aid of poly-alcohols to create a gel through esterification. The most popular chelating agent which has four carboxylate groups is ethylenediamine tetra-acetate (EDTA). After formation, the gelled composite is sintered, pyrolysing the organic species and leaving nanoparticles. In the Pechini method the metal cations are trapped in the polymer gel, while in the traditional sol–gel methods, the gel is part of the gel structure. The Pechini process uses poly-hydroxyl alcohols such as ethylene glycol

and polyvinyl alcohol as polymerizing agent in order to enhance the uniform distribution of metal ions and avoid their precipitation during evaporation [22]. Note that oxides can be prepared by the conventional acid pH Pechini process and a modified basic pH Pechini process. Higher pH of the starting solution resulted in significantly finer grains in the sintered powders. Zinc oxide (ZnO) nanorods have been successfully synthesized by modified Pechini process using ethylene glycol [23].

12.2.1.3 Precipitation Method

Precipitation processes are among the oldest of techniques for the synthesis of nanomaterials. Precipitation synthesis consists of the condensation of a solid oxide network (the precipitate) starting from soluble species. The condensation of the species is initiated by a redox reaction or by a change of pH. Precipitate containing transition-metal ions show typical colors: pink for cobalt, reddish brown for Fe^{III}, pale pink for manganese, green for nickel, etc. Different cations form precipitates at different pH values. For example, Fe commences to precipitate at $pH \approx 2.5$ as hydroxide, while at $pH \approx 1.8$ as phosphate. Zhang et al. [24] synthesized $Li_{1+x}(Ni_{1/3}Mn_{1/3}Co_{1/3})_{1-x}O_2$ powders by a two-step combustion method using the hydroxide route by mixing $(Ni_{1/3}Mn_{1/3}Co_{1/3})(OH)_2$ transition-metal hydroxides and lithium carbonate starting materials dissolved in distilled water. NaOH and NH_4OH solution was also fed into the reactor, in which the pH of the precipitate was controlled with care to its optimized value, namely $pH = 11$ [25]. After suitable grounding and stirring, the precursor was heated at 500 °C for 5 h. The final products were fired at 950 °C for 10 h in air. The mean crystallite size L_{003} in the <001> direction is about 80 Å larger than in the perpendicular direction, which is linked to the elongated shape of the crystallites. Solid solution material $0.5Li_2MnO_3$-$0.5LiNi_{0.33}Co_{0.33}Mn_{0.33}O_2$, the so-called lithium-rich compound, was prepared via a modified co-precipitation method, which takes sulfates with high solubility as the transition-metal sources of mixed hydroxide precursor [26]. This process uses desired amounts of KOH and NH_4OH, which act as a chelating agent separately fed in the reactor.

12.2.1.4 Polyol Process

The polyol process is a soft-chemical method using glycol-based solvents such as diethylene glycol (DEG), triethylene glycol (tEG), and tetraethylene glycol (TEG). The polyol process consists of the reduction of metallic compounds such as oxides and salts in a liquid alcohol medium maintained at its boiling points [27]. The action of polyol medium is twofold for the formation of monodisperse nanoparticles: a solvent and a stabilizer that limits particle growth and prohibits agglomeration. In order to achieve rapid nucleation in polyol reactions, a general rule of thumb is that

the higher the temperature of the glycol, the faster the nucleation and the more uniform the nanoparticles formed. Kim et al. [28] synthesized $LiFePO_4$ nanoparticles prepared by the polyol process without post heat treatments. The particles showed highly crystalline nature of rod and plate like morphologies with an average size of 300 nm. Badi et al. [29] reported modified polyol syntheses which produce nanocrystalline $Li_{1-y}FePO_4$ directly, where the maximum Li substoichiometry on thr M1 site sustained at synthesis temperatures of 320 °C is about 10 %. LFP nanocrystals of relatively uniform morphology were grown with an average width of 20 nm and a length of 40 nm of a very narrow particle size distribution [30].

12.2.1.5 Combustion Method

Combustion method involves exothermic redox reaction of an oxidizer (metal nitrate) and an organic fuel (carboxylic acid, carbo hydrazide (CH), oxalyl dihydrazide (ODH), tetra formal tri-azine (TFTA), acid dihydrazide, urea, etc.) to obtain the desired phase. The stoichiometry of metal nitrate to fuel is calculated assuming the complete combustion to yield metal oxide phase, and CO_2, N_2, and H_2O as by-products. Some of the fuels used were found to be specific for a particular class of oxides, e.g., urea for alumina and related oxides, carbo hydrazide for zirconia, ODH for Fe_2O_3 and ferrites, TFTA for TiO_2, glycine for chromium and related oxides [31]. Combustion synthesis can occur by two modes: self-propagating high-temperature synthesis (SHS) and volume combustion synthesis (VCS). The samples are heated by an external source either locally (SHS) or uniformly (VCS) to initiate en exothermic reaction. VCS is more appropriate for weakly exothermic ractions that require preheating prior ignition, and is sometimes referred to as "thermal explosion" mode [32]. Typical products synthesized by combustion reaction are submicron size with large surface area that both are function of the gaseous products evolved during combustion. As an example, the combustion of γ-Fe_2O_3 using a redox compound such as iron hydrazinium $FeN_2H_5(N_2H_3COO)_3$ liberates 30 mol of gases per Fe_2O_3, i.e., $6CO_2 + 8\ N_2 + 16H_2O$, whereas the redox mixture iron nitrate plus malonohydrazide $C_3H_8N_4O_2$ gives only 20 mol [33]. Julien et al. [34] prepared substituted lithium cobalt oxides, $LiCo_{0.5}M_{0.5}O_2$ (M = Ni, Mg, Mn, Zn) using urea as fuel for cathode materials in Li-ion batteries. Nanopowders 30–60 nm sized of spinel $LiMn_2O_4$ were synthesized using poly acrylic acid (PAA) [35]. The high-voltage cathode material, $LiNiVO_4$, was synthesized at temperatures as low as 320 °C using the aqueous glycine–nitrate combustion process [36]. The synthesis procedure was as follows: the aqueous solution of metal nitrate and ammonium metavanadate was mixed with glycine (aminoacetic acid) solution in the stoichiometric ratio 1:2 and heated to boiling and underwent dehydrated green-black sticky paste. This paste was decomposed at around 250 °C accompanied by a mass od small bubbles (foams) followed by the generation of combustible gases such as NO_x and ammonia, which ultimately gave rise to a pale brown powder, referred to as the precursor. The desired phase of the final product $LiNiVO_4$ was

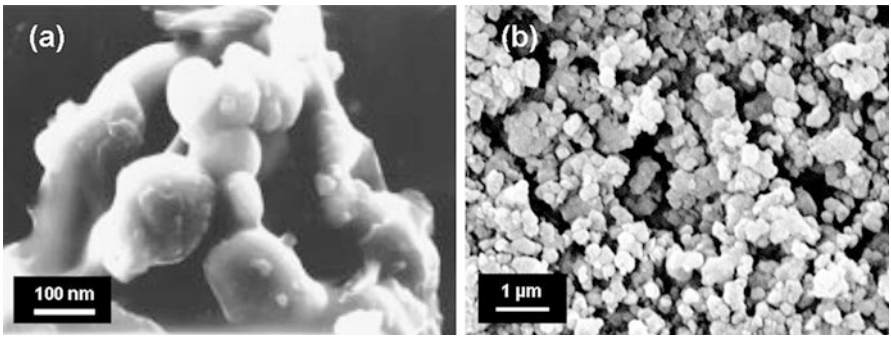

Fig. 12.3 Micrographs of (**a**) inverse spinel $LiNiVO_4$ synthesized by the glycine-assisted combustion method. (**b**) $LiMn_2O_4$ spinel nanopowders prepared by combustion method using urea as a fuel

obtained after annealing at 500 °C in air for 6 h. A theoretical reaction, assuming complete thermal decomposition of the starting materials, may be written as:

$$\begin{aligned} LiNO_{3(aq)} + Ni(NO_3)_{2(aq)} + NH_4VO_{3(aq)} + 6NH_2CH_2COOH_{(aq)} &\rightarrow^{heat}\nabla_{air} \\ \rightarrow LiNiVO_{4(s)} + 5N_{2(g)} + 12CO_{2(g)} + 17H_2O_{(g)}&. \end{aligned} \quad (12.2)$$

SEM analysis reveals the formation of spherical of spherical grains of submicronic size, average size of grains 80–180 nm (Fig. 12.3a). $LiNi_{0.3}Co_{0.7}O_2$ layered material was prepared by the glycine-assisted combustion method [37]. The carboxylic acid groups (–COOH–) that forms viscous resins act as a fuel during the crystallization process at lower temperature $T < 250$ °C providing nanostructured particles. Chitra et al. [13] have developed a new combustion method using urea as a fuel for the synthesis of spinel $LiMn_2O_4$. Nanopowders were formed around 500 °C have spherical shape (Fig. 12.3b) with nearly pore-free state and high surface area ($S_{BET} \approx 13\ cm^2\ g^{-1}$). A modified combustion synthesis, namely PVA-gel method using a solution metal nitrates containing polyvinyl alcohol (PVA) has been proposed to prepare nanostructured $LiMn_2O_4$ with loosely agglomerated spherical 30-nm sized particles [38].

12.2.1.6 Pyrolysis Method

Pyrolysis method, otherwise *wet-chemical reaction succinic acid assisted*, consists of ignition of a resin that removes the organic portion, leading the selected composition of mixed oxides chemically combined. This method with proper amount of chelating agent results in much lower calcination temperature and shorter time of calcinations and mechanically-grinding for producing single-phased nanomaterials compared with other processes. It has been found that the bulk quantities of submicron-sized particles can be obtained at a modest temperature as low as 300 °C, with the highest level of phase purity. This technique describes a simple solution mixing procedure

[39, 40]. For example, in the succinic-assisted process of $LiNi_{0.5}Co_{0.5}O_2$ the ignition occurs at 277 °C compared to 296 and 315 °C for the sol–gel and combustion method, respectively [14]. The pyrolysis method consists of metal acetates dissolved in a methanolic aqueous solution mixed with a solution of succinic acid. Care was exercised in adjusting the concentration of the complexing agent by controlling the pH of the mixed solution that forms an extremely viscous paste-like substance upon slow evaporation of methanol and acetic acid. The $(COOH)_2$ carboxylic groups of the succinic acid form chemical bonds with the metal ions in developing an extremely viscous paste-like substance upon slow evaporation of methanol and acetic acid. The paste was further dried at 120 °C to obtain the dried precursor mass. The precursor decomposition resulted in a huge exothermic reaction as exemplified by the combustion of organic species present in the precursor mass. In the case of $LiNi_{0.5}Co_{0.5}O_2$, this exothermic process yielding a brownish black colored powder enhances the oxidation reaction and onsets the phase formation of the crystalline phase. In the case of the pyrolysis synthesis of nanocrystalline $LiFePO_4$ the pH of the solution with succinic acid was adjusted, ranging between 5.0 and 5.5 using liquid NH_3 because weak acid or neutral or weak basic precursor solutions are preferable to obtain single phase $LiFePO_4$ [41] and strong basic condition should be avoided to prepare $LiFePO_4$ without impurity phase [42].

12.2.2 Template Synthesis

Ordered nanostructured materials were prepare by the template technique. This method consists of a thermal decomposition of the sol–gel precursor within the pores of a membrane. The template is dipped into the sol for 10 min and taken out for heating at $T > 400$ °C resulting in the formation of nanomaterial within the template pores. Different types of template have been widely investigated such as anodic aluminum oxides (AAO), porous polymer and nano-channel glass templates. The final nano-specimens are obtained by dissolution the template composites in 6 mol L^{-1} NaOH solution. The template method with porous membranes of AAO has been successfully used to prepare nanotubes. Li et al. [43] reported the template synthesis of $LiCoO_2$, $LiMn_2O_4$, and $LiNi_{0.8}Co_{0.2}O_2$ nanotubes by heat treatment at 500 °C for 8 h in air. Zhou et al. [44] prepared high-ordered $LiMn_2O_4$ nanowire arrays by AAO template from a polymeric matrix formed by mixture of metal acetates as the cationic sources and citric acid and ethylene glycol as the monomers. The as-produced nanowires were uniformly distributed and had a diameter of around 100 nm.

12.2.3 Spray-Pyrolysis Method

Spray-pyrolysis method is a useful method for the synthesis of high purity, narrow size distribution, homogeneous composition of oxide particles with spherical morphology.

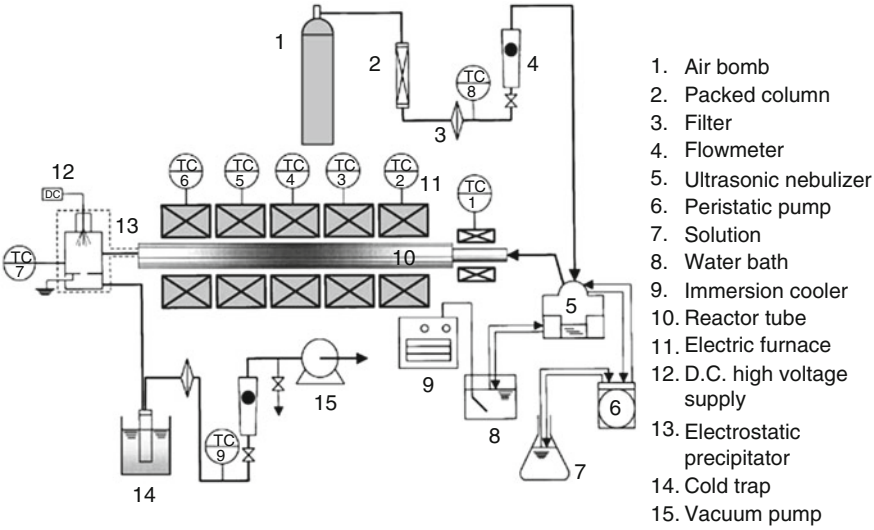

Fig 12.4 Schematic diagram of the experimental apparatus for ultrasonic spray pyrolysis synthesis. Reproduced with permission from [45]. Copyright 2002 Elsevier

The schematic diagram of the experimental apparatus is presented in Fig. 12.4. This setup is divided into three parts such as droplet generator, pyrolysis reactor, and particle collector. The droplet generator consists of an ultrasonic nebulizer, a peristaltic pump for supplying the precursor solution and thermostat circulation parts. The pyrolysis reactor tube is formed by putting a quartz tube (186 cm length) into a horizontal furnace, which is divided into five heating zones. Taniguchi et al. [45] reported that spherical spinel $LiMn_2O_4$ powders could be synthesized using this method by varying gas flow rates and temperature profiles in the reactor. The crystallite size was approximately 30 nm and the specific area of the particles ranges from 5.7 top 12.7 $m^2\ g^{-1}$. $Li[Ni_{1/3}Mn_{1/3}Co_{1/3}]O_2$ was prepared by a two-step synthesis: firstly the precursor $[Ni_{1/3}Mn_{1/3}Co_{1/3}]O_2$ was prepared using the spray method from an aqueous solution including hydrated metal nitrates and citric acid (molar ratio of total metal to citric acid fixed at 0.2) as a polymeric agent. The solution was atomized using an ultrasonic nebulizer with a resonant frequency of 1.7 MHz. The aerosol stream was introduced into the vertical quartz reactor heated at 500 °C. The flow rate of air used as a carrier gas was 10 L min^{-1}. The final products were obtained by mixing the precursor with excess amount of $LiOH{\cdot}H_2O$ followed by calcination at 900 °C. The powders consisted of polycrystalline aggregates (~500 nm) composed of 50-nm primary particles [46]. In the spray-drying method, dried particles with a desired diameter are instantly obtained by controlling the diameter of the spray nozzle. $LiNi_{1/3}Mn_{1/3}Co_{1/3}O_2$ was synthesized by mixing the aqueous solution of metal nitrates and succinic acid using an atomizing nozzle in combination with compressed air. The liquid is deposited at a rate of 100 ml min^{-1} and the spraying is carried out at a pressure of 2 MPa in the reactor maintained at 220 °C [47].

12.2.4 Hydrothermal Method

Since more than one century, hydrothermal synthesis was clearly identified as an important technology for preparation of nanometer-sized particles than can be quenched to form nanoparticle powder, or cross linked to produce nanocrystalline structures [48, 49]. Among the various synthesis approaches pursued in the fabrication of electrode materials for Li-ion batteries, the hydrothermal route is particularly successful with respect to controlling the chemical composition, crystallite size, and particle shape. Hydrothermal synthesis (HTS) is a process that utilizes single or heterogeneous phase reactions in aqueous media at elevated temperature ($T > 25\,^{\circ}\mathrm{C}$) and pressure ($p > 100$ kPa) to crystallize ceramic materials directly from solution [50]. HTS takes place in a wide variety of liquid media: aqueous- and solvent-based systems. HTS offers other advantages over conventional ceramic methods. All forms of nanoscale materials can be prepared, namely nanopowders [51], nanofibers [52], nanobelts [53], nanoplates [54], nanowires [55], nanorods [56], nanovesicles [57], etc. The use of inexpensive, environmentally benign water as a solvent offers a "green" manufacturing approach for large-scale production of Li(Fe,Mn)PO_4/C cathodes for high-power hybrid electric vehicle and plug-in hybrid electric vehicle applications. Further energy-consuming processing steps are reduced such as longer time high temperature calcination. HTS eliminates the formation of agglomerates and produces nanoparticles with narrow particle size distribution. Precise well-defined powder morphology can be also significant. Another merit is that the purity of hydrothermally prepared powders significantly exceeds the purity of the starting substances because the hydrothermal crystallization is a self-purifying process that rejects impurities. However, the conventional hydrothermal process involves a longer reaction time. For instance, it is 5–12 h to synthesize $LiFePO_4$ [58–60]. In this regard, microwave-assisted synthesis approaches will be appealing because they can shorten the reaction time to a few minutes with significant energy savings. The one-pot synthesis was developed for preparing Li$M$$PO_4$/C ($M$ = Mn, Fe, Co) nanocomposites by a microwave assisted hydrothermal process involving hydrothermal carbonization of glucose [61]. Recently, Beninati et al. [62] and Wang et al. [63] reported the synthesis of $LiFePO_4$ by irradiating the solid-state raw materials with carbon in a domestic microwave oven. An in situ coating of carbon on $LiFePO_4$ was attempted during the MW-HT process, employing glucose as the carbon source. An aqueous solution of LiOH, H_3PO_4, and glucose was first stirred for a few minutes. An aqueous solution of the sulfates of Mn^{2+}, Fe^{2+}, or Co^{2+} was then added to this mixture so that the Li:M:P molar ratio was 3:1:1 and the M^{2+} to glucose molar ratio was 2:1, which resulted in a carbon content of 5 wt% in the final product. Although, the synthesis of transition-metal oxides or olivine phosphates requests a careful control of the pH of the solution. Reaction mixtures are acidic for M = Mn (pH = 6.1) and Fe (pH = 6.7), while they are kept basic (pH = 9.9) for M = Co by adding ammonium hydroxide. Because cobalt phosphate hydrate without lithium is known to be formed under acidic conditions for M = Co, a basic condition was employed to obtain $LiCoPO_4$ [64]. During the synthesis of $LiFePO_4$, the pH

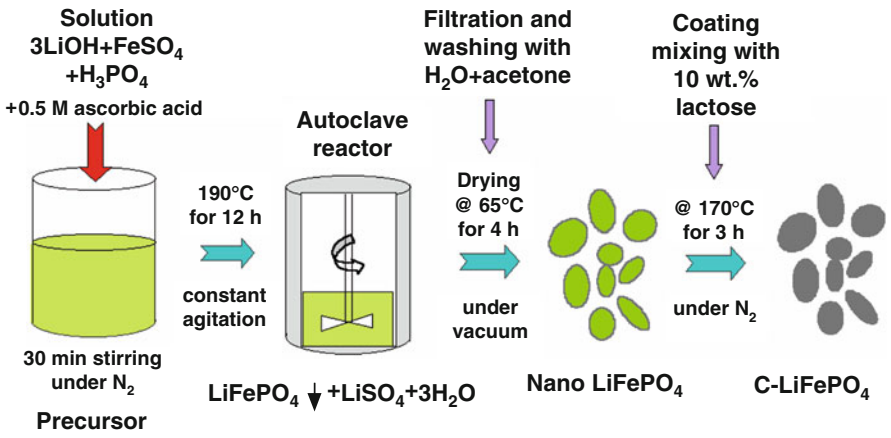

Fig. 12.5 Schematic picture of synthesis procedure of LFP particles using a stirring hydrothermal method

value of the reaction precursor solution was measured before and after hydrothermal synthesis. Supercritical hydrothermal synthesis introduces organic ligands (amino acids, carboxylic acids, or alcohols) into supercritical hydrothermal conditions, in which the water is in a state above the critical temperature (374 °C) and pressure (22.1 MPa). Because the drastic change in density, the solubility is greatly enhanced and phase behavior changes largely around the critical point. Consequently particle size is in the range from 2.5 to 10 nm and particle size dispersion is extremely narrow. Crystal shape can be controlled by changing concentration of organic modifiers such as nanosphere and nanocube [64]. Numerous investigations have been devoted to synthesize electrode materials for Li-ion batteries such as $LiFePO_4$ [65], $LiMn_2O_4$ [66], $LiCoO_2$ [67], and $Li_4Ti_5O_{12}$ [68].

$LiFePO_4$-C cathode materials were prepared by hydrothermal synthesis assisted by rotating/stirring tests at different agitation speeds (Fig. 12.5) [69]. The hydrothermal processes were carried out at 190 °C for 12 h with a solution chemistry of $LiOH{\cdot}H_2O$, $FeSO_4 \cdot 7H_2O$, H_3PO_4 (85 wt%), and ascorbic acid (as reducing agent) in the stoichiometry 3Li:1Fe:1P:0.2C. Annealing was done at 700 °C under nitrogen atmosphere using lactose as carbon coating source. The $LiFePO_4$-C electrodes prepared by employing agitation during hydrothermal synthesis were found to exhibit higher discharge capacities (137.6 mAh g^{-1} at *C*/12) than those prepared without agitation (106.2 mAh g^{-1}). This was equally true for higher current rates, namely *C*/5 and *C*/3. Via a series of tests at different speeds (260–1150 rpm) and different concentrations (0.4, 0.5, 0.6 mol dm^{-3}) the optimum solution rotating agitation/concentration conditions were determined to be 260–380 rpm and 0.5 mol dm^{-3}, respectively. Under these conditions $LiFePO_4$-C materials with excellent capacity retention (~130 mAh g^{-1} at coulombic efficiency >99 %), and better cycling stability at high current rates (1*C*) were obtained. The improved performance of the $LiFePO_4$-C material obtained by controlled rotating

agitation-hydrothermal solution synthesis is attributed to production of less aggregated particles with high surface area and less impurity. Hence, the controlled rotating agitation solution synthesis method provides a scalable and eco-friendly way in producing better performing cathode particles for use in Li-ion batteries [69].

12.2.5 Jet Milling

Micronization of materials is a common process in many aspects of manufacturing pharmaceuticals, toners, ceramics, cosmetics, and paints. The principle of micronization by jet milling is the collision of particles within a fast gas jet. The processes responsible for size reduction and separation within the milling chamber were investigated intensively in the 1960s by Rumpf and Kuerten [70]. Although much is known on the particle size reduction of hard and crystalline materials, the jet milling is a grinding process of using highly compressed air or other gases, usually in a vortex motion, to impact fine particles against each other in a chamber [71–74]. This technique involves a grinding energy created by gas streams from horizontal grinding air nozzles, whose main interest is the very low pollution of ground powders. It allows the production of very fine powders with relatively hard materials. The principle is as follows. The sample material is sucked into a grinding chamber. Jets of compressed air or another inert gas accelerate the particles which collide in an area of maximum turbulence. The powders are then recovered by cyclone systems. This technique has some advantages: small particle size, particle spherical and uniform, grinding materials temperature-sensitive, low pollution of ground powders, tight particle size control, large and small batch quantities, easy cleaning and maintenance of the mill (Fig. 12.6).

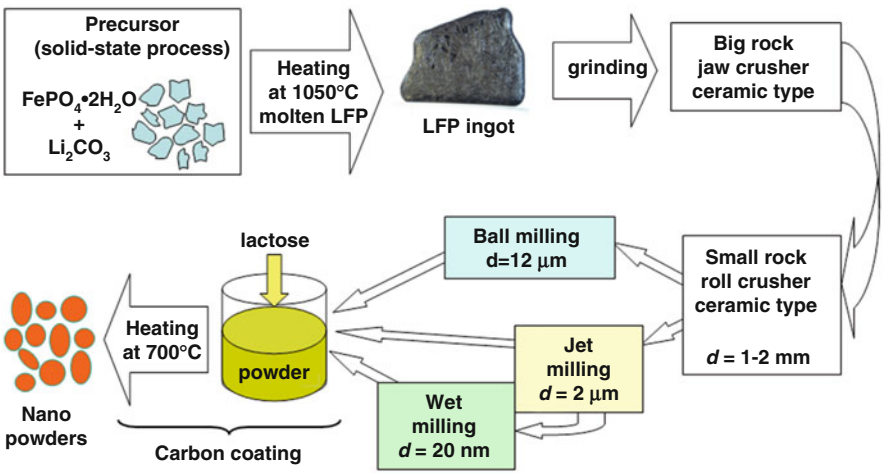

Fig. 12.6 Synthesis from molten ingot. Nanopowders are obtained using crusher ceramic liner and jet milling

$LiFePO_4$ (LFP) nanoparticles have been obtained by grinding ingot synthesized in the molten state (Fig. 12.6). This process, followed by jet milling, and then wet milling, provides a simple way to obtain powders with monitored size of the particles in the whole range from macroscopic to 25 nm, although at this stage, we find that these particles tend to segregate to form secondary particles of size ~100 nm [75]. The synthesis procedure was as follows. First, the ingot obtained by heating a mixture $FePO_4{\cdot}2H_2O$ and Li_2CO_3 at 1050 °C for 5 min and cooled in Ar atmosphere. Then the ingot was crashed into centimeter-sized particles by using a jaw-crusher with ceramic liner to avoid metal contamination. The third process used a roll crusher (ceramic type) to obtain millimeter-sized particles. The millimeter-sized particles are further ground by using jet-mill to achieve micrometer-sized particles. In the process, the grains enter the grading wheel and are blasted to cyclone separator and collector. The smallest particle size (25 nm) was reached by jet milling of microsized particles dispersed in isopropyl alcohol (IPA) solution at 15 % of solid concentration and ground on a bead mill using 0.2 mm zironial's beads. Finally the carbon-coating was realized by mixing nanoparticles with carbon precursor (lactose) in acetone solution after drying, the blend is heated at 700 °C for 45 h in neutral atmosphere [75]. Core–shell nanostructured xLi_2MnO_3 $(1-x)LiMO_2$ (M = Ni, Co, Mn) composite cathode materials were synthesized through a simple solid-state reaction using a mechanochemical ball-milling process [76]. TEM analysis shows primary particles smaller (<100 nm) than of the starting material because the low temperature synthesis (~400 °C) of the Li_2MnO_3 powders.

12.3 The Disordered Surface Layer

12.3.1 General Considerations

The increase of rate capability of cathode materials (for use in hybrid electric vehicles for instance) could be achieved by decreasing as much as possible the size of the particles to improve the effective surface that is active for electrochemical reactions. In addition, smaller size means reduced path for the electrons and the Li^+ ions inside the particles. Since the electronic and ionic conductivity are small [30], this reduction is expected to benefit the performance, especially at high C-rates. The experimental results, however, are not as simple as one might have expected, because the reduction in size implies that surface effects become more important, and the surface layer does not necessarily have the same properties as the bulk, with important impact on the electrochemical properties. The bulk properties (i.e., physical and chemical properties big enough so that surface effects are negligible) are now well understood. That is not the case, yet, for surface effects that are still under debate.

Several experiments have evidenced the existence of a disordered layer (DSL) at the surface of particles of oxide, typically few nanometers that modified the intrinsic properties of electrode material for Li-ion batteries [77–83]. Yet attention must be

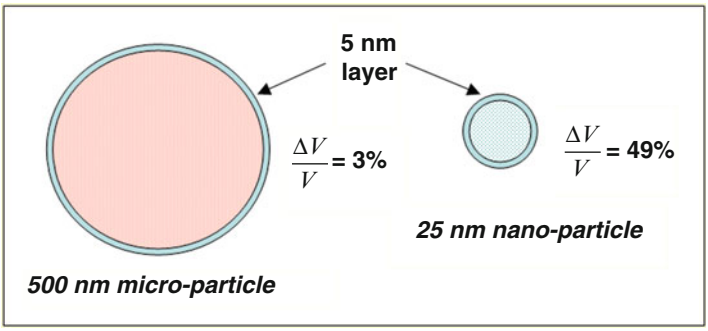

Fig. 12.7 Schematic representation of the simple core–shell model for description of the importance of the disordered surface layer in nanoparticle

paid to the quality of the surface, especially as the importance of the surface-to-volume ratio increases for nanomaterials, in order to prevent the surface from acting as a barrier to transfer of lithium ions and/or electrons during the charging and discharging of lithium batteries. Figure 12.7 depicts a simple model of the shell–core volume ratio, R_{SC}, for a 5-nm thick surface layer: in the case of a big enough particle (0.5 μm diameter) $R_{SC} = 3$ %, while it becomes 49 % for a nanoparticle (25 nm diameter). In this context, it is obvious that the nanoparticle behaves differently than the big one. Aurbach et al. [84] have suggested that the capacity retention of a cathode active material is strongly dependent on the surface chemistry of the particles of the insertion material, which are always covered by surface films limiting the Li-ion migration and their charge transfer across the active interface.

To illustrate this complex situation, let see the case of olivine material. In particular, the phase diagram of Li_xFePO_4 shows that the solid solution is unstable at room temperature for big particles (say, particles of size $d \geq 100$ nm). As a consequence, a rapid demixing occurs upon cooling, and we are left with two phases, namely $Li_{1-\alpha}FePO_4$ and $Li_\beta FePO_4$, where α, β denote the width of the single-phase regions [85]. Yet these parameters are small for large particles, say of diameter $d \leq 100$ nm, in which case, in first approximation, the lithiation–delithiation process involves $xLiFePO_4 + (1-x)FePO_4$ and not Li_xFePO_4 solid solutions. This separation, which takes its origin in Coulomb correlation [86], has an important impact on electrochemical properties, since it results in the plateau Li^0/Li^+ voltage vs. x at 3.4 V. However, upon decreasing the size of the particles, experiments reported in the literature show that the plateau is shrinking, which has been interpreted as the sign that the miscibility gap decreases with d. This has been confirmed by Gibot et al. [87] according to which the voltage plateau is no longer observed in particles with $d \approx 40$ nm. Amorphizationn of the particle was observed upon cycling for crystallite size in the range $d \leq 100$ nm, which has been interpreted in terms of nucleation limited phase transition pathways [88]. This amorphization, however, has not been observed in particles of size $d \approx 100$ nm, in which case well crystallized $LiFePO_4$ and $FePO_4$ domains have been observed at any stage of lithiation/delithiation process [89].

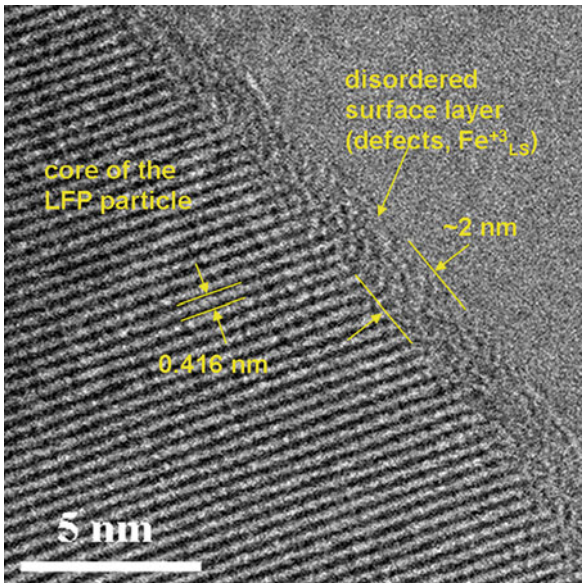

Fig. 12.8 HRTEM image showing the disordered surface layer for an as-prepared $LiFePO_4$ particle

High-resolution transmission electronic microscope (HRTEM) image (Fig. 12.8) shows that a surface layer of about 2-nm thick is strongly disordered, but not amorphous [77]. Note that the core of the particles below the surface has a size that is the same as the coherence length deduced from the XRD analysis. Therefore, the particles are crystallites surrounded by a disordered surface layer. The HRTEM image after carbon coating shows the same particle, now covered with a 3-nm thick carbon layer, and a less-disordered surface layer. It is now possible to investigate the role of the carbon coating by comparison of the physical and chemical properties between the $LiFePO_4$ particles before and after carbon coating [80]. Since the surface layer is only about 3 nm wide and not well ordered, however, XRD experiments are not sensitive to the surface layer. The investigation of the magnetic properties is a good strategy for this purpose, since iron is a magnetic ion. In the bulk, iron is known to be in the Fe^{2+} high spin state and thus carries the spin $S = 5/2$ (the orbital momentum is quenched by the crystal field and is thus negligible). The magnetic properties associated to the spin of a given iron ion are quite sensitive to its local environment. That is why they can be used as a probe of any defect or impurity in its vicinity. This strategy was successful for the bulk [5], but also for the surface [77], with which we are concerned hereunder.

12.3.2 DSL of $LiFePO_4$ Nanoparticles

The preparation and characterization of nanoparticles of $LiFePO_4$ is then of primary importance, in as much as their structural properties may depend on their size.

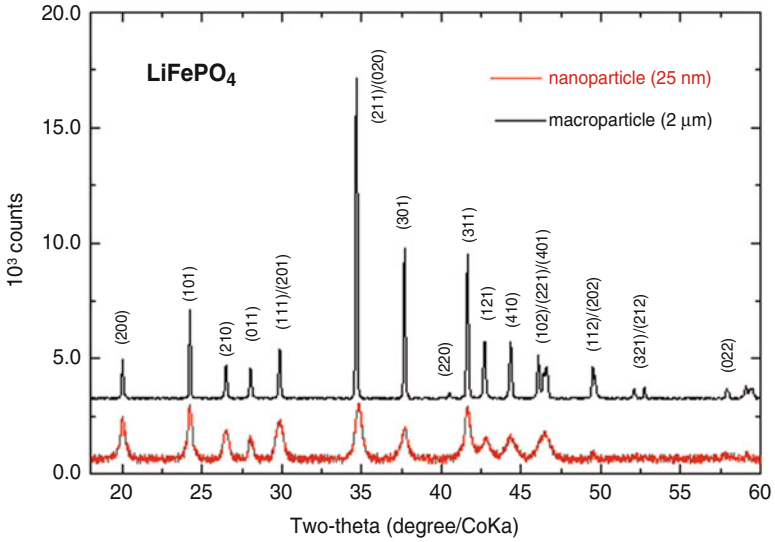

Fig. 12.9 XRD patterns of $LiFePO_4$ sample with primary particles 25 nm size, secondary particles of size 100 nm (*lower spectrum*) obtained after jet milling and of sample with 2-µm particle size (*upper spectrum*) for comparison

$LiFePO_4$ particles of sizes in the range 30–40 nm have been prepared by jet-milling route with carbon coating for optimization of the electrochemical performance [75]. The XRD pattern of 25-nm sized nanoparticles is shown in Fig. 12.9 with the spectrum of particle of 2 µm for comparison. The local structure was studied by FTIR spectroscopy of the samples obtained just after roll, jet and wet milling as shown in Fig. 12.10. The positions of the intrinsic bands in the spectra of $LiFePO_4$ are well known: the bands in the range 372–647 cm^{-1} are bending modes (ν_2 and ν_4) involving $(PO_4)^{3-}$ symmetric and asymmetric modes and Li vibrations, while the part of the spectrum in the range 945–1139 cm^{-1} corresponds to the stretching modes of the $(PO_4)^{3-}$ units. They involve symmetric and asymmetric modes of the P–O bonds at frequencies closely related to those of the free molecule. There is a band broadening as d increases: the most resolved spectra are observed in the wet-milled case. The broadening is the signature to a shorter lifetime of the vibration modes due to solid friction associated to defects. The more resolved spectrum observed for smaller values of d is then attributable to the fact that smaller particles have less structural defects such as grain boundaries in the vicinity of which the lattice is less ordered (in the limit of nanoparticles $d = 25$ nm, the particles are also crystallites ($d \approx l$), and thus without any structural defect in the bulk of the particles). The only disorder for such small particles is located in the surface layer, inside which the iron ions are in the Fe^{3+} low spin ($S = 1/2$) configuration. The disorder is found to have dramatic effects on the electrochemical properties as it stabilizes the solid solution inside the passivation layer. This disorder is strongly reduced by the carbon coating at 750 °C, which switches the

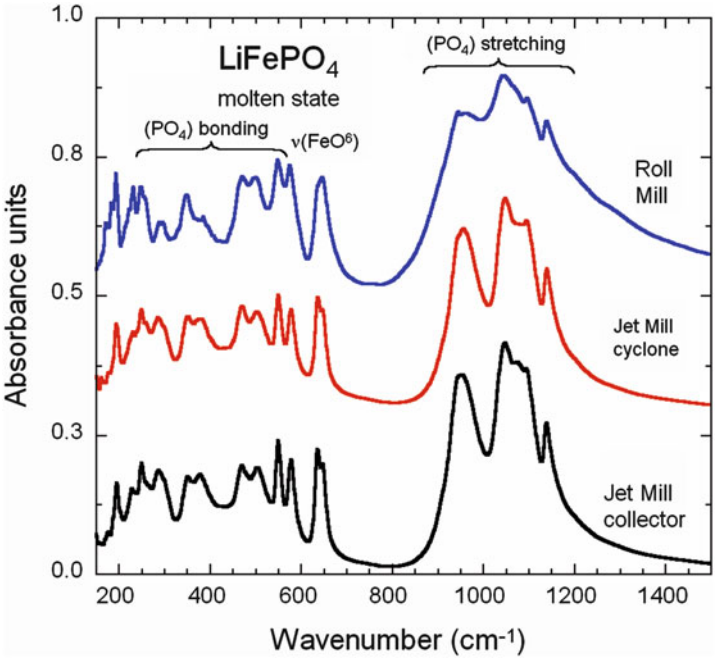

Fig 12.10 FTIR absorption spectra of molten-state samples at different stages of the grinding process (before carbon coating): roll mill, jet mill cyclone, and jet mill collector

Fe^{3+} ions in the surface layer to the high spin ($S = 5/2$) configuration, and restores the plateau of the voltage vs. capacity. The results are discussed in the context of the controversy on the shrinking of the miscibility gap upon decreasing the size of the particles to the nanoscale.

For nanoparticles, the fraction $(1 - y)$ of iron ions in the surface layer is not negligible, and we found that this contribution is different from that of the bulk that was investigated by magnetic measurements [80]. The response of the magnetic moments of the iron ions is thus different for the ions in the bulk and the ions in the surface layer. Therefore, one has to add to the bulk contribution to the magnetic susceptibility the contribution coming from the iron ions inside the surface layer (Fig. 12.11). We found that this contribution satisfies the Curie law, so that $\chi(T)$ takes the form:

$$\chi(T) = y\,\frac{C_0}{T + \theta_0} + (1 - y)\,\frac{C'}{T}, \tag{12.3}$$

for $T \geq 100$ K. There are two fitting parameters, the fraction y of iron ions in the bulk, and C'. We have shown that the solution for the set (y, C') is unique, and for particles with diameter 40 nm, it is [75]:

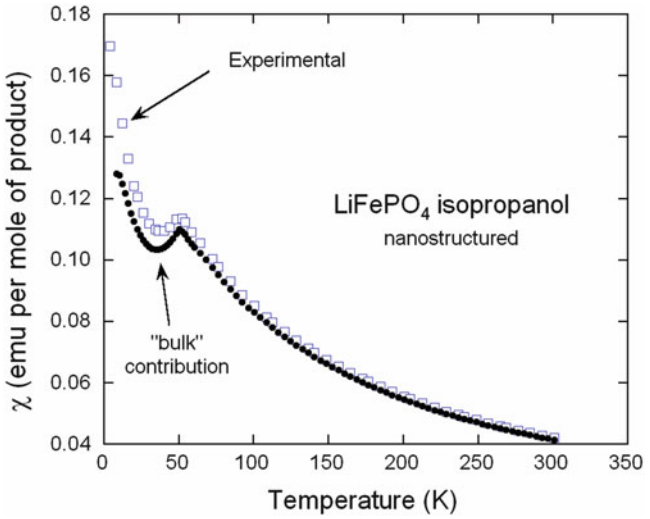

Fig. 12.11 Magnetic susceptibility of $LiFePO_4$. The *solid circles* are the contribution of the core region, and match the results observed for particles without surface effects. The *open squares* are experimental data for the 40 nm sized particles before carbon coating. The difference is quantitatively fit by the second term in Eq. (12.3)

$$y = 0.89,\ C^{'} = 0.37 \text{ emu K mol}^{-1}. \tag{12.4}$$

It should be noticed that the contribution of the core region to the magnetic susceptibility reduced to the Curie–Weiss expression only in the paramagnetic regime. On the other hand, the absence of spin correlations evidenced by the Curie law implies that, at any temperature, including below the Néel temperature T_N:

$$\chi(T) - \chi_{\text{bulk}}(T) = (1-y)\frac{C^{'}}{T}, \forall T, \tag{12.5}$$

which has been verified [75]. This behavior at low temperature allows us to distinguish between the increase of the effective moment due to the magnetic polarons (investigated in the previous section) and surface effects, since the polarons care spin-frozen at low temperature and do not give a Curie contribution to the susceptibility. The value of y is self-consistent with the ratio N_S/N_B, with N_S the number of iron ions in the 3-nm thick surface layer and N_B the number of iron ions in the core region of a spherical particle of 40 nm in diameter. The value of C', however, was not necessarily expected, as it corresponds to a spin $S = 1/2$, implying that iron in the surface layer of uncoated particles is Fe^{3+} in the low spin state. On this example, the magnetic properties of uncoated particles have revealed important properties. First of all, the iron in the surface layer is trivalent. A significant amount of Fe^{3+} is systematically detected in $LiFePO_4$ by Mössbauer experiments although they do not give any information on their location [5]. The magnetic properties are

the first evidence that these Fe^{3+} ions are localized in the surface layer. In addition, the analysis of $\chi(T)$ has shown that the Fe^{3+} ions are uncorrelated, since there contribution is a Curie law C'/T with vanishing Curie–Weiss temperature (at least down to 10 K). This is the evidence for important frustration of the magnetic interactions in the surface layer: the decorrelation of the magnetic spins is the translation on the magnetic properties of the structural disorder that affects the surface layer. Finally, the Fe^{3+} ions are in the low-spin state. Remember that a free ion, i.e., ion not submitted to the crystal field, is always in the high spin state due to the Hund's rule. The low spin state is then signature that the crystal field is big enough to break the Hund's rule. This is another signature of an important structural disorder that enhances crystal-field effects in the surface layer. The fact that the iron ions are in the trivalent state means that the surface layer has been delithiated.

After carbon coating, the magnetic response of the coated particles is closer to the result predicted for intrinsic $LiFePO_4$ with, however, an effective moment 5.02 μ_B still slightly larger than the theoretical value 4.90 μ_B. Since Fe^{3+} in the high-spin state is 5/2, its effective moment is 5.92, and we note that:

$$y(4.9)^2 + (1-y)(5.92)^2 = (5.02)^2, \tag{12.6}$$

which means that the excess in magnetic moment with respect to the theoretical value is entirely attributable to the conversion of $Fe^{3+}(S = 1/2)$ in $Fe^{3+}(S = 5/2)$ in the surface layer. This is actually the "normal" state for iron in the surface layer. In particular, we have shown that exposure to moisture, even for short period of time, oxidizes the iron at the surface, with the consequence that iron is in the $Fe^{3+}(S = 5/2)$ in the surface layer. Note that the study of the degradation of the particles upon exposure to moisture has shown that the surface layer is completely delithiated very fast, but after that, no further delithiation is observed at the scale of few days because the $FePO_4$ surface layer is waterproof and protects the core [78]. The same magnetic analysis has been performed on lamellar compounds, and they have shown that the exposure to moisture induces a delithiation over a thickness of 10 nm in that case [81], larger than the 3 nm in $LiFePO_4$, so that the lamellar compounds are more sensitive to moisture than olive samples.

12.3.3 DSL of $LiMO_2$ Layered Compounds

Actually, not even the transition-metal oxides, but also carbon coating is efficient to improve the cycle life of Li-ion batteries with $LiN_{1/3}Mn_{1/3}Co_{1/3}O_2$ (NMC) and $LiCoO_2$ (LCO) as well. Even a simple heating in presence of an organic compound is sufficient because it has an annealing effect that re-crystallizes the surface layer that is otherwise disordered. The surface of NMC particles were studied for material synthesized at 900 °C by a two-step process from a mixture of $LiOH{\cdot}H_2O$ and metal oxalate $[(Ni_{1/3}Co_{1/3}Mn_{1/3})C_2O_4]$ obtained by co-precipitation [82]. The effect of the

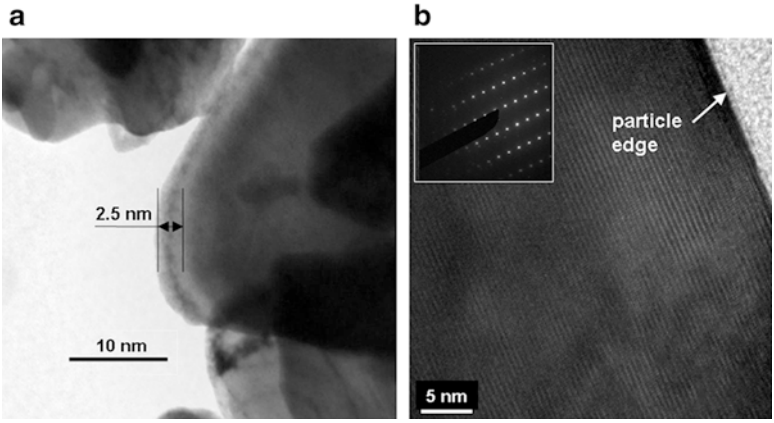

Fig. 12.12 TEM images of NMC powders showing the surface modification of 250-nm sized particle. Images (**a**) and (**b**) display the HRTEM features of NMC powders for as-grown and heat treated sample with sucrose at 600 °C for 30 min in air, respectively. Reproduced with permission from [82]. Copyright 2011 Elsevier

heat treatment at 600 °C with organic substances, such as sucrose and starch, investigated by HRTEM images and Raman spectra, indicate that the surface of particles has been modified. The annealing process does not lead to any carbon coating but it leads to the crystallization of the thin disordered layer on the surface of NMC. The analysis of the HRTEM images (Fig. 12.12) gives evidence that the surface of the particles have been modified by the calcination at 600 °C. Before carbon treatment, we observe the presence of an amorphous-like layer, typically 2.5-nm thick that covers the NMC particle. In the micrograph, this surface layer appears as a greyish region at the edge of NMC crystallites, while the core of the primary particle is the dark region. After the heat-treatment at moderate temperature with an organic substance such as sucrose or starch, we observe the disappearance of disordered layer. Thus the edge of the particle displays well-defined election diffraction patterns (insert of Fig. 12.12). The beneficial effect has been tested on the electrochemical properties of the NMC cathode materials in half lithium cell. For rate performance comparison, the modified Peukert plots, i.e., the specific capacity vs. *C*-rate, are shown in Fig. 12.13. A capacity 107 mAh g^{-1} is delivered in the voltage range 2.5–4.2 V at 10*C* rate from the cell with surface-modified NMC, while it is only 81 mAh g^{-1} with the non-treated NMC electrode at the same *C*-rate.

The effect of H_2O on NMC in humid atmosphere was investigated by structural, magnetic and electrochemical analysis on $LiNi_{1/3}Mn_{1/3}Co_{1/3}O_2$ (NMC) compounds synthesized by the co-precipitation method [81]. The consequence is that immersion of NMC to H_2O and exposure of NMC to humid atmosphere led to a rapid attack that manifests itself by the delithiation of the surface layer of the particles. This aging process occurred during the first few minutes, then it is saturated, and the thickness of the surface layer at saturation is 10 nm. The quantitative analysis of the Raman spectrum of NMC samples was reported in ref. [81]. Upon exposure to ambient atmosphere for 1 day, the spectrum of the same sample shows three

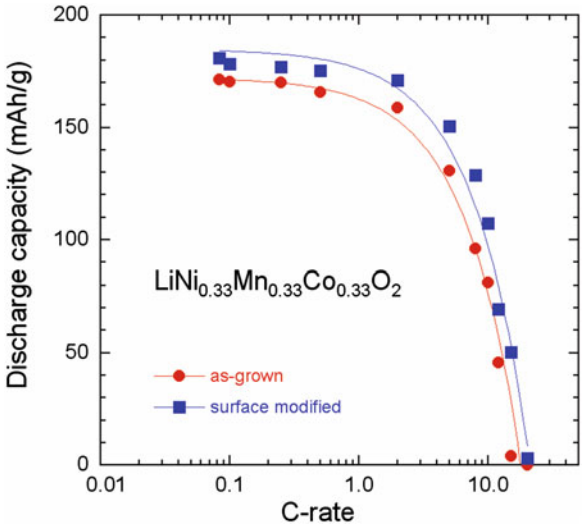

Fig. 12.13 Modified Peukert plots of Li//NMC coin cells for the as-grown and the surface modified NMC cathode material. Reproduced with permission from [82]. Copyright 2011 Elsevier

additional bands that are characteristic of LiOH, and another band characteristic of CO_3 molecular unit, which confirms the presence of Li_2CO_3 in addition of the lithium hydroxide. The general trend in intercalation compounds is recovered, whether they are lamellar or not, according to which the reaction of lithium with H_2O at the surface results in the delithiation of the surface layer, the lithium involved in the process forming LiOH and Li_2CO_3 at the surface. The degradation of the surface of $LiNi_{1/3}Mn_{1/3}Co_{1/3}O_2$ affects the electrochemical properties of the material as a cathode element. After aging, an initial discharge capacity of 139 mAh g^{-1} was delivered at 1*C*-rate in the cutoff voltage of 3.0–4.3 V. About 95 % of its initial capacity was retained after 30 cycles.

12.4 Electrochemical Properties of Nanoparticles

In this section, first we present the effect of surface modification by carbon coating of $LiFePO_4$ nanoparticles and secondly the comparison between energy- and power-grade LFP materials. Figure 12.14 shows the typical charge–discharge voltage profile of the $LiFePO_4$ cathode material investigated here before carbon coating (a) and after carbon-coating (b), using LFP/$LiPF_6$-EC-DEC/Li cell. The test was performed galvanostatically at charge–discharge rate *C*/24 that is very slow, to insure that equilibrium has been reached. The voltage range is 2.2–4.0 V vs. Li^0/Li^+. The charge–discharge profile appears with the typical voltage plateau (at ca. 3.45 V vs. Li^0/Li^+) attributed to the two-phase reaction $FePO_4$-$LiFePO_4$ system. However, the plateau has been shrunk, especially on the side of low Li concentrations (charged state). However, after carbon-coating, the full width of the plateau has been

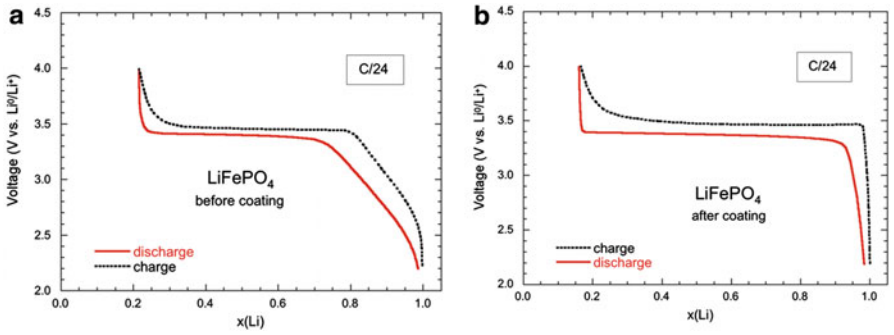

Fig. 12.14 Charge–discharge voltage profile of $LiFePO_4$ before (**a**) and after (**b**) carbon coating cathode material using LFP/$LiPF_6$-EC-DEC/Li cell at room temperature. The test was performed galvanostatically at charge–discharge rate *C*/24

recovered. The carbon-coated material exhibits a reversible capacity 160 mAh g^{-1} that amounts to a utilization efficiency of 94 %. Zaghib et al. [77] shed light on the conflicting results found by different groups on the phase diagram and electrochemical properties of $LiFePO_4$ particles of size $d \approx 40$ nm. Degraded electrochemical properties and slope in the charge–discharge profile are due to the stabilization of the solid solution, in the region of the particle where a sever disorder exists. With the synthesis process we have used, in the present work, this region is limited to the surface layer only, before carbon-coating. On the other hand, the treatment associated to the carbon-coating cures this disorder, so that we have obtained particles well crystallized and free from impurity and defect. For such particles, we find, in agreement with theoretical models that the small size of the particles has not modified significantly the electrochemical properties of material. Since in addition, the aggregation of the particles is small and the dispersion of the particles is small, this synthesis process opens the route to the preparation of nano-structured particles of $LiFePO_4$ for use as the active element in future Li-ion batteries with high power.

Figure 12.15 displays the SEM images of two types of LFP particles: LFP synthesized by solid-state reaction via the polymer-precursor method showing particles of 2–5 μm size and LFP synthesized by hydrothermal method showing particles with an average size of 300 nm. The modified Peukert plots are shown in Fig. 12.16. It is remarkable that the power-grade powders 75 % of the initial capacity at 10*C*-rate.

12.5 Nanoscale Functional Materials

12.5.1 WO_3 Nanocomposites

Tungsten trioxide is an n-type semiconductor which has found a great deal of interest in several applications including electrochromic displays, smart windows,

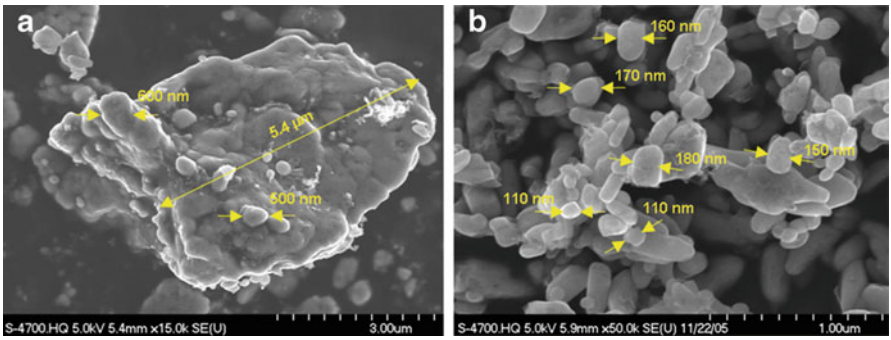

Fig. 12.15 SEM images of $LiFePO_4$ powders. (**a**) Energy grade and (**b**) power grade powders

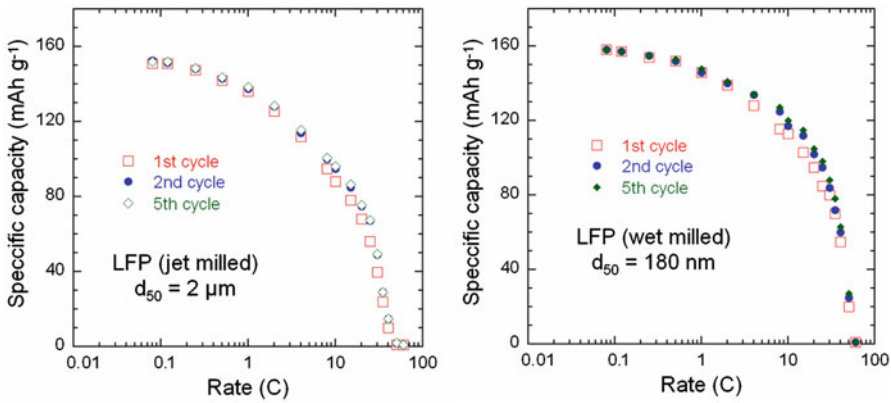

Fig. 12.16 Modified Peukert plots of $LiFePO_4$ cathode materials as a function of the particle size: (*left*) energy grade and (*right*) power grade powders

gas detectors, and electrochemical capacitors. The optimal performance of the WO_3 nanomaterials in the sensor devices depends on the electrical conductivity and surface adsorption properties, which are closely related to the structure, morphology and size of the particles. Ag-doped WO_3 nanomaterials have been studied as sensing element to detect relative humidity (RH) with an average sensitivity of 2.14 MW%RH in the 20–90 % range. The Ag:WO_3 bronze was prepared by soft-chemical route with 147-nm particle size [90]. WO_3 nanomaterials were synthesized via a sol–gel method and calcination for use as a CO gas sensor. The sensitivity of WO_3 sensor ships was determined by comparing the changes in electrical resistance in the absence and presence of 50 ppm of CO gas at 200 °C [91]. Nanocrystalline WO_3 films prepared by gas evaporation show enhanced gas-sensing properties; when doped with Al or Au, 5 ppm of H_2S yielded a conductance increase by ~250 times even at room temperature [92].

Among materials for electrochromic display devices (ECDs), WO_3 has attracted the most attention, so far. It is well-known that better electrochromic reversibility and relatively short response time depends on the structure and morphology of the films. An attempt at surface modification of WO_3 films and enhancement of the diffusion rate of Li ions in an electrochromic device was realized using by incorporating nanoscopic silicon oxide particles into WO_{3-x}-0.1TiO_2 thin films prepared by the sol–gel route, which exhibit increase of lifetime and stability. The sol–gel solution with nano-sized SiO_2 particles (40 nm) was spin-coated onto indium-tin-oxide covered glass substrate [93]. The variation of the optical density of surface-developed of WO_{3-x}-0.1TiO_2 thin films during coloring ($E = -2.5$ V) and bleaching ($E = +1.5$ V) was studied in lithium cell using nonaqueous electrolyte of 1 mol L^{-1} $LiClO_4$ in propylene carbonate. Saturation of the coloration is almost reached after 1.5 s for the nanocomposite films, while pure WO_{3-x} takes ≈ 4 s. The improvement of specific charge density from $Q = 9.4$–41 mC cm^{-2} observed for pure and surface developed films could be explained as follows (1). The response time is improved due to the extremely high surface area of the composite, leading to the enhancement of ion insertion through the film–electrolyte interface (2). The presence of SiO_2 nanoparticle results a more open xerogel amorphous structure of WO_{3-x} films. This is the enhancement effect that has been observed in the ionic conduction of LiI-Al_2O_3 composite [94].

12.5.2 WO_3 Nanorods

The Li-driven electrochemical properties of monoclinic WO_3 nanorods prepared by a solution-base colloidal approach have been studied and the relationship between the properties and the nano-structures of the materials has been established [95]. WO_3 nanorods with a high aspect ratio were found to yield an intercalation capacity up to 1.12 Li per formula unit, much higher than the value of 0.78 Li for bulk WO_3. This can be explained on the basis of the unique rod-like structure that effectively enhanced structure stability. The evolution of Li-driven reaction kinetics further illustrated benefits of WO_3 nanorods owing to the increased edge and corner effects. WO_3 nanorods were synthesis by using hydrothermal process without any surfactants. The nanorod film deposited on ITO exhibits high electrochromic stability and comparable color display, contrast, and coloration/bleaching response. The maximum transmittance wave-lengths have obvious blue-shifts and the transmittance intensities decrease with the increase of the applied negative voltages within the spectra of 500–900 nm. The electrochromic device was cycled more than 3000 cycles with a coloration/bleaching response of 8 s [96].

12.5.3 WO_3 Nanopowders and Nanofilms

Different forms of nanomaterials were synthesized for optical applications in lithium-based devices. Mixed WO_3–TiO_2 oxides have been prepared from aqueous solutions of tungstic acid and titanium isopropoxide in H_2O_2. Peroxopolytungstic acids were obtained from pure tungstic acid whereas $WO_3 \cdot 1/3H_2O$ is formed in the presence of Ti^{VI}. Three crystalline oxides are formed successively upon heating Ti doped $WO_3 \cdot 1/3H_2O$, namely h-WO_3, o-WO_3, and m-WO_3. The intermediate metastable o-WO_3 phase has not been observed in the absence of titanium. The cathodic behavior of these oxides shows that the discharge curves corresponding to the electrochemical insertion of Li are noticeably different [97, 98]. In the course of the preparation of WO_3 by sol–gel technique, kinetics of its synthesis and the structural changes were studied by in situ Raman spectroscopy during the transition from colloidal solution to gel. The removal of water molecules affects the symmetric W = O stretching mode. The Raman spectrum of a gelified sample shows peaks attributed to the O-W-O bending mode and the disappearance of the high-frequency mode attributed to polyanionic species. After 2 days the gelified sample became a precipitated material, which exhibited the Raman spectrum of a crystalline tungsten oxide hydrate [99]. Another potential application of WO_3 thin films is in aerospace industry for infrared emissivity modulation and temperature control in spacecraft [100]. WO_3 500-nm thick films were fabricated by the pulsed-laser deposition (PLD) technique. The compositional studies using X-ray photoelectron spectroscopy and electron probe microanalysis (EPMA) measurements indicated that the grown films were nearly stoichiometric with small amount of oxygen vacancies. Figure 12.17a shows the bright field TEM image of the sample structure. The morphology of the PLD WO_3 films is characterized by the grains of 60–70 nm in size and root-mean-square (rms) surface roughness value of 10 nm. HRTEM image (Fig. 12.17b) confirms that the film consists of a well-crystallized WO_3, which is identified as the monoclinic phase [101].

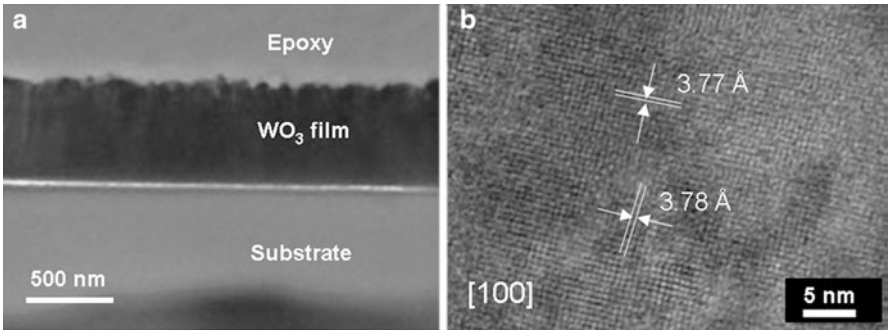

Fig. 12.17 Electron micrographs of WO_3 thin films. Image (**a**) is the bright field view of the sample structure. The substrate, the WO_3 thin film, and the epoxy regions are indicated in the micrograph. Image (**b**) is the HRTEM image of the WO_3 thin film with lattice fringes corresponding to the monoclinic structure

12.5.4 Li_2MnO_3 Rock-Salt Nano-structure

Among the lithium insertion oxides, Li_2MnO_3 is one of the most interesting compounds from the point of view of its structure and electrochemical behavior [102, 103]. Indeed, this oxide, in its microcrystalline form, is electrochemically inactive for lithium insertion and extraction between 2.0 and 4.4 V; however it delivers a high theoretical capacity of 460 mAh g^{-1} for total Li extraction. Li_2MnO_3 (or alternatively $Li[Li_{1/3}Mn_{2/3}]O_2$) has a rock-salt structure containing layers of Li^+ and Mn^{4+} cations between close-packed arrays of oxygen anions; all the octahedral sites are occupied by cations. A layer of lithium ions and a mixed layer of (1:2) lithium and manganese ions alternate between close-packed oxygen layers (see the structural representation in Fig. 5.24). This compound is electrochemically inactive. Insertion of Li^+ ions into a stoichiometric rock-salt phase is not possible because all the octahedral sites are fully occupied. Li extraction is not energetically feasible because all the manganese cations are tetravalent. Nanoparticles (20–80 nm) of Li_2MnO_3 were synthesized using the self-combustion reaction and studied the electrochemical activity of electrodes prepared from this nano-material at 30, 45, and 60 °C [103]. It was shown that the first Li-extraction from nano-Li_2MnO_3 occurs at much lower potentials (by 180–360 mV) in comparison with micron-sized Li_2MnO_3 electrodes. This can be associated with the higher surface-to-volume ratio, much shorter the diffusion path and the increased surface concentration of the electrochemically active sites. Figure 12.18 shows a comparison of the XRD patterns from the nano-sized Li_2MnO_3 material with that obtained from the micron-sized Li_2MnO_3 material. The nano-sized material is characterized by significant broadening of the peaks.

On the basis of magnetic susceptibility studies of nano-Li_2MnO_3 we proposed a model of disordered surface layer, containing Mn^{3+} or Mn^{2+} ions, both at low spin state, at the surface of these nanoparticles. From the results of structural analysis

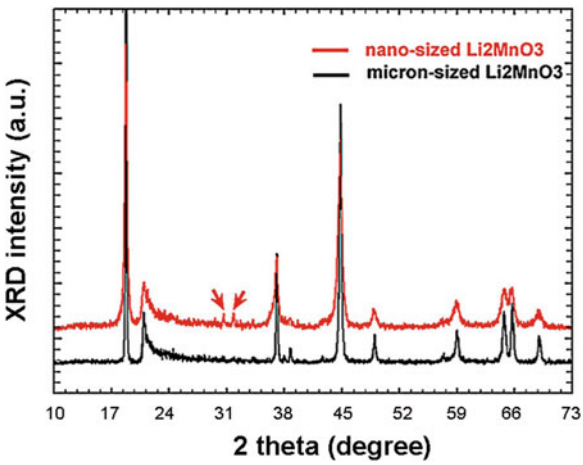

Fig. 12.18 The XRD patterns of nano-sized Li_2MnO_3 (*upper curve*) compared with micron-sized material (*lower curve*). Two peaks marked by arrows at $2\theta = 30.5$ and 31.6° belong to Li_2CO_3 impurity that can be formed during the synthesis due to some excess of the lithium

(by X-ray and electron diffraction and vibrational Raman spectroscopy) of galvanostatically cycled nano-Li_2MnO_3 electrodes in Li-cells we came to a conclusion of partial transition of layered $LiMnO_2$ to spinel-type ordering during delithiation/lithiation. This was confirmed also by analysis of Raman spectroscopy of these materials that demonstrated a strong blue-shift of the main Raman band (A_{1g} mode) attributed to formation of the spinel-type structural ordering.

12.5.5 *Aluminum Doping Effect in NCA Materials*

Aluminum doped $LiNi_yCo_{1-y}O_2$ (NCA) oxides prepared by wet-chemical method from citrate precursor displays a nano-structured phase. The influence of Al doping on particle size and morphologies is clearly evidenced in Fig. 12.19. The net result of incorporation of a small amount of 0.05 mol% Al is the decrease of the grain size from 300 nm for $LiNi_{0.7}Co_{0.3}O_2$ to 80 nm for $LiNi_{0.70}Co_{0.25}Al_{0.05}O_2$. In addition the particle size distribution is narrow. XRD patterns show that the doped sample belongs to the $LiNiO_2$-$LiCoO_2$-$LiAlO_2$ solid solution and has the layered rhombohedral structure ($R\bar{3}m$ S.G.).

The charge–discharge profiles of Li//$LiNi_{0.70}Co_{0.25}Al_{0.05}O_2$ and Li//$LiCoO_2$ cells in the potential range 2.5–4.3 V are shown in Fig. 12.19. Replacing a small amount of Co demonstrates higher capacity retention compared with $LiCoO_2$ electrode (≈50 mV) At cutoff voltage of 4.3 V ($\Delta x = 0.72$), the specific capacity delivered by the Li//$Li_xNi_{0.6}Co_{0.35}Al_{0.05}O_2$ cell is ca. 195 mAh g^{-1}, which is a larger value than the Li//Li_xCoO_2 system with $\Delta x = 0.5$. Due to the nanosized particle the capacity retention is less than NCA materials with $y = 0.7$. The trends for the Al^{3+}-doped materials show that lower capacities were obtained with an increase in y(Al) because Al^{3+} cation cannot be oxidized, so it is an

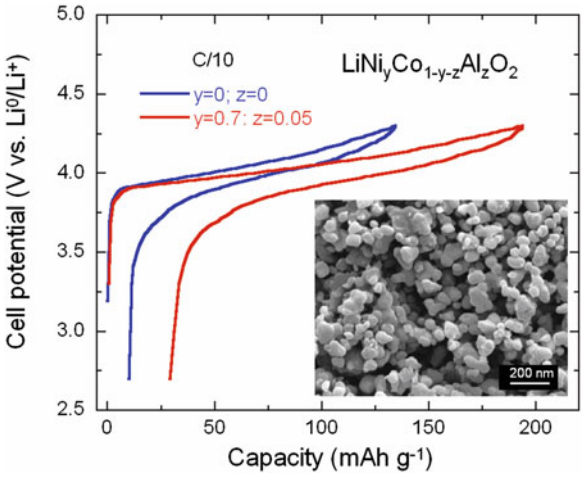

Fig. 12.19 First charge–discharge curve of the Li//$LiNi_{0.70}Co_{0.25}Al_{0.05}O_2$ cell compared with the voltage-composition profile of Li//$LiCoO_2$. The insert shows the SEM image of NCA powders

electrochemically inactive element. Long life electrochemical data showed that the cell using $LiNi_{0.70}Co_{0.25}Al_{0.05}O_2$ powders performed slightly better than the other ones. This means that for Al^{3+} doping, the optimum doping level for gravimetric capacity and life cycle ability would be approximately $y = 0.05$. No reason could be given for such a trend. However, the rechargeability of the $Li//LiNi_{0.70}Co_{0.25}Al_{0.05}O_2$ cells seems better than $LiCoO_2$ because the lack of the two-phase behavior in the high voltage region ($x \approx 0.5$). In addition, the electronic resistivity of the cathode material increases at the end of the charge, which is an advantageous property for preventing overcharge. Thus safety appears to be better with Al-doped $LiNi_yCo_{1-y}O_2$ for fully charge state when Li ions cannot be extracted from the host matrix because no electrons are removed from either Al^{+3} or Co^{4+} state [104, 105].

12.5.6 MnO_2 Nanorods

As an important inorganic compound, MnO_2 has been extensively used in many fields including primary batteries, lithium batteries, water treatment, supercapacitors, sensors, because its specific chemical structures and physical properties. Attractive features for implementing MnO_2 based materials for battery applications is the low cost, and also a highly abundant transition metal compared to for example cobalt, nickel, and vanadium. Hence, MnO_2-type batteries are attractive for energy storage applications like electric vehicles that require large amounts of materials in the market [106]. Substituted MDO nanowires with various elements, Cr, Al, Ni and Co, were prepared through the redox reactions of solid-state precursors or ion-adduct precursors under hydrothermal or non-hydrothermal condition. It was found that the partial replacement of Mn with transition-metal ions could improve the electrode performance of 1D-nanostructured manganates [107]. Nanosized pure, Ag-coated and doped manganese dioxides (MDO) were prepared through a redox reaction between $KMnO_4$ and fumaric acid. XRD analysis showed cryptomelane crystal structure for pure, coated and doped α-phases. Chemical analysis detected the presence of silver in doped and coated MDO. Scanning electron microscope and energy-dispersive spectroscopy analyses confirmed the presence of silver in doped and coated oxides. TEM images showed that the pure MnO_2 particles were synthesized in nanoscale with about 20 nm and agreed with calculated value by Scherrer's formula. From the representative TEM image (Fig. 12.20a) doped-MnO_2 sample has a rod-like shape. The average size of these nanorods is about 25 nm in diameter and 90 nm in length. Magnetic measurements showed reduction in Mn^{3+} ions in the crystal structure after coating and doping with silver. The electrochemical performance showed that Ag-coated and doped MnO_2 samples have better initial capacities than pristine MnO_2. Ag-coated MnO_2 material

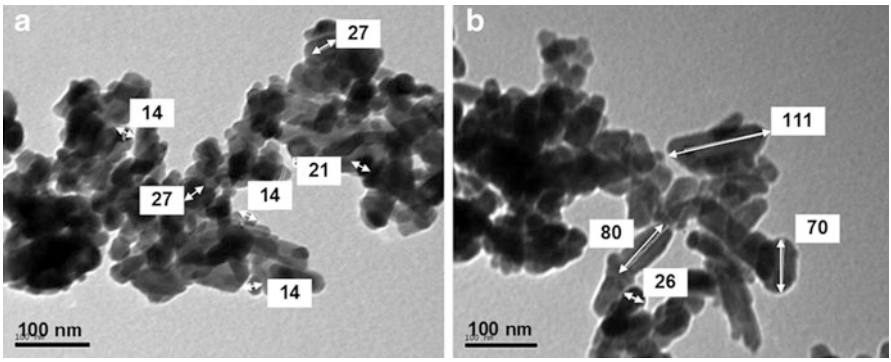

Fig. 12.20 TEM images of (**a**) Ag-coated and (**b**) Ag-doped nanorod-like MnO_2 prepared by redox reaction between $KMnO_4$ and fumaric acid

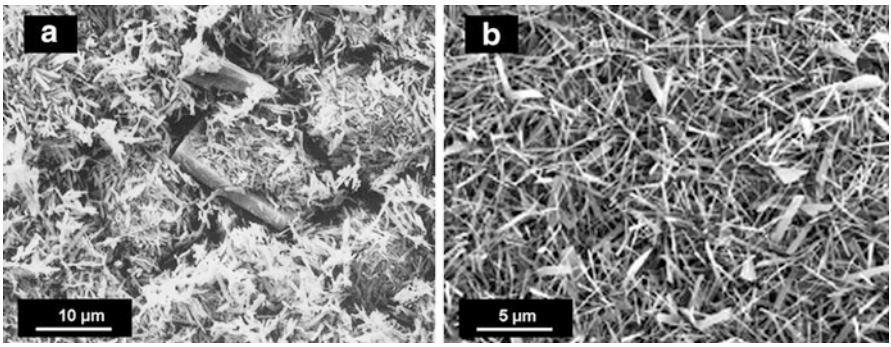

Fig. 12.21 SEM images of (**a**) The intermediate compound was placed in the autoclave heated at 170 °C and (**b**) The nanofibers synthesized in the autoclave heated at 185 °C for 6 days

showed the best capacity retention upon cycling among all prepared MnO_2 oxides, i.e., 140 mAh g^{-1} after the 40th cycle at *C*/5 rate in the potential window 1.5–4.0 V vs. Li^0/Li^+ [56, 108].

12.5.7 MoO_3 Nanofibers

MoO_3 nanofibers were synthesized by hydrothermal reaction from acidified ammonium heptamolybdate tetrahydrate precursor (Fig. 12.21). Structural analysis shows that MoO_3 nanofibers 50–80 nm in diameter and a several micrometers in length are crystallized with the α-form in the orthorhombic system (*Pbnm* S.G.). The composition $MoO_{2.9975}$ was determined by Rietveld refinement and magnetic susceptibility measurements. The electrochemical performance of Li//MoO_3 cells with

nanofibers deliver a better discharge capacity after 40 cycles than MoO_3 bulk. Nanofibers show a specific capacity 265 mAh g^{-1} for the first discharge in the potential range 3.5–1.5 V with Li uptake of 1.5 Li/Mo. Thus, the electrochemical features of nanofibers are characteristic of a two-phase domain similar to that of bulk α-MoO_3. However, we notice that, as expected, the discharge curve exhibits larger cell polarization for high *C*-rate, i.e., about 0.6 V at 2*C*. Structural evolution of this domain corresponds to a solid solution involving $Li_{0.08}MoO_3$ and $Li_{0.2}MoO_3$ (called α′-MoO_3). The evolution of the local structure of cathode materials during the first discharge has been studied by Raman spectroscopy. Results describe that the lithium insertion process consists in rather moderate local distortions allowing the accommodation of 1.5 Li/mol of oxide without breaking of the orthorhombic symmetry [109].

12.6 Concluding Remarks

One of the challenges in the field of rechargeable lithium-ion batteries is the use of nanoparticles for cathode and anode materials. This in general should be considered as favorable for achieving high rate capability, since solid-state Li-ion transport in the bulk materials may be the rate-determining step for the entire intercalation–deintercalation processes. The use of nanoparticles leads to reducing to minimum the diffusion path for the electrons and the Li-ion transport, and to better accommodation of strain during Li^+ extraction/insertion. Furthermore, since the electrochemical active surface area is inversely proportional to the particle size, the electrodes comprising nanoparticles posses significantly larger surface area and have more active sites for the electrochemical reactions. Hence for nanoparticles, surface effects become more important than the bulk properties and they are still under debate in the literature. In regard of the materials for positive electrodes in lithium cells, it was demonstrated that the cathodes comprising nanoparticles of $LiMn_{0.5}Ni_{0.5}O_2$ and $LiMn_{1.5}Ni_{0.5}O_4$ display faster kinetics than electrodes based on micrometric-size particles. It was also shown that the electrodes prepared from the spinel $LiMn_2O_4$ nanoparticles exhibited improved cycling performance, small charge-transfer resistance at the electrode–solution interface, a reduced the Jahn–Teller effect, and stabilization of the nano-$LiMn_2O_4$ cathodes in cycling at 60 °C. In the case of nano-crystalline $LiCoO_2$ electrodes, the increased values of the discharge capacity were attributed to shorter diffusion distances that promote faster and more uniform Li^+ intercalation. The dramatic effect of the small grain-size material (<20 nm) on increasing the electrochemical activity (capacity) has been established recently for the lithium extraction/insertion reactions of $LiCrO_2$ electrodes. On the other hand, nanoparticles with a relatively high surface area may be reactive with electrolyte solutions based on alkyl carbonate solvents and $LiPF_6$

(which unavoidably contain detrimental contaminants such as HF, trace water, PF_5 and POF_3). Possible reactions with solution species may develop undesirable detrimental side reactions (especially on the high surface area particles) leading to the passivation phenomena and high electrode impedance. In these systems, the irreversible oxidation of alkyl carbonate solvents resulting in the evolution of CO_2 accompanies the electrochemical processes at high anodic potentials. For more than a decade, researchers have accumulated lots of information and reported numerous papers on the synthesis of nanoparticles of the lithiated transition-metal oxides, their magnetic properties, vibrational modes studied by infra-red and Raman spectroscopy, and on the electrochemical performance of positive electrodes comprising nanoparticles of the active material in lithium cells. Based on the literature reports in the field, it can be concluded that the possible use of nanomaterials in electrodes for Li-ion batteries should be studied rigorously and specially for each electrode material individually taking into account the balance between the pros and cons. In regard of the Li_2MnO_3 nanoparticles, we realized that the literature data on their characterization and electrochemical performance are scarce. It was shown, for instance that the electrochemical behavior of the nanocrystalline Li_2MnO_3 electrodes depends upon the particles morphology, specific surface area, and annealing temperature of the as-prepared material. The authors synthesized nano-Li_2MnO_3 by the solid-state reaction and studied the structural transformation of this material between layered $LiMnO_2$ and cubic $LiMn_2O_4$ spinel-type phases.

References

1. Feynman RP (1992) There's plenty of room at the bottom. J Microelectromech Syst 1:60–66
2. Zaghib K, Julien CM, Prakash J (2003) New trends in intercalation compounds for energy storage and conversion. The Electrochem Society, Pennington
3. Chen Z, Dahn JR (2002) Reducing carbon in $LiFePO_4$/C composite electrodes to maximize specific energy, volumetric energy and tap density. J Electrochem Soc 149:A1184–A1189
4. Weppner W, Huggins RA (1977) Determination of the kinetic parameters of mixed-conducting electrodes and application to the system Li_3Sb. J Electrochem Soc 124:1569–1578
5. Julien CM, Mauger A, Ait-Salah A, Massot M, Gendron F, Zaghib K (2007) Nanoscopic scale studies of $LiFePO_4$ as cathode material in lithium-ion batteries for HEV application. Ionics 13:395–411
6. Ravet N, Goodenough J.B, Besner S, Simoneau M, Hovington P, Armand M (1999) Improved iron based cathode material. In: Proceedings of the 196th ECS meeting, Honolulu, extended abstract n° 127. Accessed Oct 1999
7. Lalena JN, Clearly DA (2010) Principles of inorganic materials design. Wiley, Hoboken, NJ
8. Huang B, Jang YI, Chiang YM, Sadoway DR (1998) Electrochemical evaluation of $LiCoO_2$ synthesized by decomposition and intercalation of hydroxides for lithium-ion battery applications. J Appl Electrochem 28:1365–1369

9. Julien C, El-Farh L, Rangan S, Massot M (1999) Synthesis of $LiNi_{1-y}Co_yO_2$ cathode materials prepared by a citric acid-assisted sol-gel method for lithium batteries. J Sol Gel Sci Technol 15:63–72
10. Abdel-Ghany AE, Hashem AM, Abuzeid HA, Eid AE, Bayoumi HA, Julien CM (2009) Synthesis, structure characterization and magnetic properties of nanosized $LiCo_{1-y}Ni_yO_2$ prepared by sol-gel citric acid route. Ionics 15:49–59
11. Garcia B, Barboux P, Ribot F, Kahn-Harari A, Mazerolles L, Baffier N (1995) The structure of low temperature crystallized $LiCoO_2$. Solid state Ionics 80:111–118
12. Myung ST, Kim GH, Sun YK (2004) Synthesis of $Li[Ni_{1/3}Co_{1/3}Mn_{1/3}]O_{2-z}F_z$ via coprecipitation. Chem Lett 33:1388–1389
13. Chitra S, Kalyani P, Mohan T, Gangadharan R, Yebka B, Castro-Garcia S, Massot M, Julien C, Eddrief M (1999) Characterization and electrochemical studies of $LiMn_2O_4$ cathode materials prepared by combustion method. J Electroceram 3:433–441
14. Julien C, Letranchant C, Rangan S, Lemal M, Ziolkiewicz S, Castro-Garcıa S, El-Farh L, Benkaddour M (2000) Layered $LiNi_{0.5}Co_{0.5}O_2$ cathode materials grown by soft-chemistry via various solution methods. Mater Sci Eng B 76:145–155
15. Azib T, Ammar S, Nowak S, Lau-Truing S, Groult H, Zaghib K, Mauger A, Julien CM (2012) Crystallinity of nano C-$LiFePO_4$ prepared by the polyol process. J Power Sourc 217:220–228
16. Liu W, Farrington GC, Chaput F, Dunn B (1996) Synthesis and electrochemical studies of spinel phase $LiMn_2O_4$ cathode materials prepared by the Pechini process. J Electrochem Soc 143:879–884
17. Vivekanandhan S, Venkateswarlu M, Satyanarayana N (2005) Effect of different ethylene glycol precursors on the Pechini process for the synthesis of nano-crystalline $LiNi_{0.5}Co_{0.5}VO_4$ powders. Mater Chem Phys 91:54–59
18. Kwon SW, Park SB, Seo G, Hwang ST (1998) Preparation of lithium aluminate via polymeric precursor routes. J Nucl Mater 257:172–179
19. Pereira-Ramos JP (1995) Electrochemical properties of cathodic materials synthesized by low-temperature techniques. J Power Sourc 54:120–126
20. Taguchi H, Yoshioka H, Matsuda D, Nagao M (1993) Crystal structure of $LaMnO_{3+\delta}$ synthesized using poly(acrylic acid). J Solid State Chem 104:460–463
21. Pechini MP (1967) Method of preparing lead and alkaline-earth titanates and niobates and coating method using the same to form a capacitor. US Patent 3,330,697. Accessed 11 Jul 1967
22. Tai LW, Lessing PA (1992) Modified resin-intermediate processing of perovskite powders: part I. Optimization of polymeric precursors. J Mater Res 7:511–519
23. Ramasamy Devaraj R, Karthikeyan K, Jeyasubramanian K (2013) Synthesis and properties of ZnO nanorods by modified Pechini process. Appl Nanosci 3:37–40
24. Zhang X, Jiang WJ, Mauger A, Qi L, Gendron F, Julien CM (2010) Minimization of the cation mixing in $Li_x(NMC)_{1-x}O_2$ as cathode materials. J Power Sourc 195:1292–1301
25. Lee KS, Myung ST, Prakash J, Yashiro H, Sun YK (2008) Optimization of microwave synthesis of $Li[Ni_{0.4}Co_{0.2}Mn_{0.4}]O_2$ as a positive electrode material for lithium batteries. Electrochim Acta 53:3065–3074
26. Chen Y, Xu G, Li J, Zhang Y, Chen Z, Kang F (2013) High capacity $0.5Li_2MnO_3$-$0.5LiNi_{0.33}Co_{0.33}Mn_{0.33}O_2$ cathode material via a fast co-precipitation method. Electrochim Acta 87:686–692
27. Larcher D, Patrice R (2000) Preparation of metallic powders and alloys in polyol media: a thermodynamic approach. J Solid State Chem 154:405–411
28. Kim DH, Kim TR, Im JS, Kang JW, Kim J (2007) A new method to synthesize olivine phosphate nanoparticles. J Phys Scripta T 129:31–34
29. Badi SP, Wagemaker M, Ellis BL, Singh DP, Borghols WJH, Kan WH, Ryan DH, Mulder FM, Nazar LF (2011) Direct synthesis of nanocrystalline $Li_{0.90}FePO_4$: observation of phase segregation of anti-site defects on delithiation. J Mater Chem 21:10085–10093

30. Kim DH, Kim J (2006) Synthesis of $LiFePO_4$ nanoparticles in polyol medium and their electrochemical properties. Electrochem Solid State Lett 9:A439–A442
31. Patil KC, Aruna ST, Mimani T (2002) Combustion synthesis: an update. Curr Opinion Solid State Mater Sci 6:507–512
32. Varma A, Rogachev AS, Mukasyan AS, Stephen Hwang S (1998) Combustion synthesis of advanced materials: principles and applications. Adv Chem Eng 24:79–226
33. Patil KC (1993) Advanved ceramics: combustion synthesis and properties. Bull Mater Sci 16:533–541
34. Julien C, Camacho-Lopez MA, Mohan T, Chitra S, Kalayani P, Gopakumar S (2001) Combustion synthesis and characterization of substituted lithium cobalt oxides in lithium batteries. Solid State Ionics 141–142:549–557
35. Hyu-Bum P, Kim J, Chi-Woo L (2001) Synthesis of $LiMn_2O_4$ powder by auto-ignited combustion of poly(acrylic acid)-metal nitrate precursor. J Power Sourc 92:124–130
36. Prabaharan SRS, Michael MS, Radhakrishna S, Julien C (1997) Novel low-temperature synthesis and characeterization of $LiNiVO_4$ for high-voltage Li ion batteries. J Mater Chem 7:1791–1796
37. Julien C, Michael SS, Ziolkiewicz S (1999) Structural and electrochemical properties of $LiNi_{0.3}Co_{0.7}O_2$ synthesized by different low-temperature techniques. Int J Inorg Mater 1:29–37
38. Lu CH, Saha SK (2001) Low temperature synthesis of nano-sized lithium manganese oxide powder by the sol-gel process using PVA. J Sol Gel Sci Technol 20:27–34
39. Prabaharan SRS, Saparil NB, Michael SS, Massot M, Julien C (1998) Soft chemistry synthesis of electrochemically-active spinel $LiMn_2O_4$ for Li-ion batteries. Solid State Ionics 112:25–34
40. Julien C (2000) 4-Volt cathode materials for rechargeable lithium batteries, wet-chemistry synthesis, structure and electrochemistry. Ionics 6:30–46
41. Higuchi M, Katayama K, Azuma Y, Yukawa M, Suhara M (2003) Synthesis of $LiFePO_4$ cathode material by microwave processing. J Power Sourc 119:258–261
42. Lee J, Teja AS (2005) Characteristics of lithium iron phosphate ($LiFePO_4$) particles synthesized in subcritical and supercritical water. J Supercrit Fluids 35:83–90
43. Li X, Cheng F, Guo B, Chen J (2005) Template-synthesized of $LiCoO_2$, $LiMn_2O_4$ and $LiNi_{0.8}Co_{0.2}O_2$ nanotubes as the cathode materials of lithium ion batteries. J Phys Chem B 109:14017–014024
44. Zhou YK, Shen CM, Huang J, Li HL (2002) Synthesis of high-ordered $LiMn_2O_4$ nanowire arrays by AAO template and its structural properties. Mater Sci Eng B 95:77–82
45. Taniguchi T, Song D, Wakihara M (2002) Electrochemical properties of $LiM_{1/6}Mn_{11/6}O_4$ (M = Mn, Co, Al, and Ni) as cathode materials for Li-ion batteries prepared by ultrasonic spray pyrolysis method. J Power Sourc 109:333–339
46. Park SH, Yoon CS, Kang SG, Kim HS, Moon SI, Sun YK (2004) Synthesis and structural characterization of layered $Li[Ni_{1/3}Mn_{1/3}Co_{1/3}]O_2$ cathode material by ultrasonic spray pyrolysis method. Electrochim Acta 49:557–563
47. Guo ZP, Liu H, Liu HK, Dou SX (2003) Characterization of layered $LiNi_{1/3}Mn_{1/3}Co_{1/3}O_2$ cathode materials prepared by spray-drying method. J New Mat Electrochem Syst 6:263–266
48. Byrappa K, Yoshimura M (2001) Handbook of hydrothermal technology. William Andrew Publishing, Norwich
49. Yoshimura M, Suchanek WL, Byrappa K (2000) Soft solution processing: a strategy for one-step processing of advanced inorganic materials. MRS Bull 25:17–25
50. Suchanek WL, Riman RE (2006) Hydrothermal synthesis of advanced ceramic powders. Adv Sci Technol 45:184–193
51. Brochu F, Guerfi A, Trottier J, Kopeć M, Mauger A, Groult H, Julien CM, Zaghib K (2012) Structure and electrochemistry of scaling nano C-$LiFePO_4$ synthesized by hydrothermal route: complexing agent effect. J Power Sourc 214:1–6

52. Eftekhari A (2006) Bundled nanofibers of V-doped $LiMn_2O_4$ spinel. Solid State Commun 140:391–394
53. Ma R, Bando Y, Zhang L, Sasaki T (2004) Layered MnO_2 nanobelts: hydrothermal synthesis and electrochemical measurements. Adv Mater 16:918–922
54. Xiao X, Liu X, Wang L, Zhao H, Hu Z, He X, Li Y (2012) $LiCoO_2$ nanoplates with exposed (001) planes and high rate capability for lithium-ion batteries. Nano Res 5:395–401
55. Xiao X, Yang L, Zhao H, Hu Z, Li Y (2012) Facile synthesis of $LiCoO_2$ nanowires with high electrochemical performance. Nano Res 5:27–32
56. Hashem AM, Abuzeid HM, Abdel-Latif AM, Abbas HM, Ehrenberg H, Indris S, Mauger A, Groult H, Julien CM (2013) MnO_2 nanorods prepared by redox reaction as cathodes in lithium batteries. ECS Trans 50–24:125–130
57. Li Q, Gao F, Zhao D (2002) One-step synthesis and assembly of copper sulphide nanoparticles to nanowires, nanotubes and nanovesicles by a simple organic amine-assisted hydrothermal process. Nano Lett 2:725–728
58. Shiraishi K, Dokko K, Kanamura K (2005) Formation of impurities on phospho-olivine $LiFePO_4$ during hydrothermal synthesis. J Power Sourc 146:555–558
59. Lee J, Teja AS (2006) Synthesis of $LiFePO_4$ micro and nanoparticles in supercritical water. Mater Lett 60:2105–2109
60. Jun B, Gu HB (2008) Preparation and characterization of $LiFePO_4$ cathode materials by hydrothermal method. Solid State Ionics 178:1907–1914
61. Vadivel-Murugan A, Muraliganth T, Manthiram A (2009) One-pot microwave-hydrothermal synthesis and characterization of carbon-coated $LiMPO_4$/C (M=Mn, Fe, Co) cathodes. J Electrochem Soc 156:A79–A83
62. Beninati S, Damen L, Mastragostino M (2008) MW-assisted synthesis of $LiFePO_4$ for high power applications. J Power Sourc 180:875–879
63. Wang L, Huang Y, Jiang R, Jia D (2007) Preparation and characterization of nano-sized $LiFePO_4$ by low heating solid-state coordination method and microwave heating. Electrochim Acta 52:6778–6783
64. Hayashi H, Hakuta Y (2010) Hydrothermal synthesis of metal oxide nanoparticles in supercritical water. Materials 3:3794–3817
65. Xu CB, Lee J, Teja AS (2008) Continuous hydrothermal synthesis of lithium iron phosphate particles in subcritical and supercritical water. J Supercrit Fluid 44:92–97
66. Lee JH, Ham JY (2006) Synthesis of manganese oxide particles in supercritical water. Korean J Chem Eng 23:714–719
67. Shin YH, Koo SM, Kim DS, Lee YH, Veriansyah B, Kim J, Lee YW (2009) Continuous hydrothermal synthesis of HT-$LiCoO_2$ in supercritical water. J Supercrit Fluids 50:250–256
68. Zhu W, Yang M, Yang X, Xu X, Xie J, Li Z (2014) Supercritical continuous hydrothermal synthesis of lithium titanate anode materials for lithium-ion batteries. US Patent 20140105811 A1. Accessed 17 Apr 2014
69. Vediappan K, Guerfi A, Gariépy V, Demopoulos GP, Hovington P, Trottier J, Mauger A, Julien CM, Zaghib K (2014) Stirring effect in hydrothermal synthesis of C-$LiFePO_4$. J Power Sourc 266:99–106
70. Kuerten H, Rumpf H (1966) Zerkleinerungsuntersuchungen mit tribolumineszierenden Stoffen. Chemie Ing Techn 38:331–342
71. Tanaka T, Kanda Y (2006) Crushing and grinding. In: Masuda H, Higashitani K, Yoshida H (eds) Powder technology handbook, vol 3. CRC Taylor and Francis, New York
72. Saleem IY, Smyth HDC (2010) Micronization of a soft material: air-jet and micro-ball milling. AAPS Pharm Sci Tech 11:1642–1649
73. Hosokawa Micron Powder Systems (1996) Fluidized bed jet milling for economical powder processing. Ceram Ind. http://hmicronpowder.com/fluidized.pdf. Accessed Apr 1996
74. Comex (2014) Jet milling. http://www.comex-group.com/Comex/files/78/Brochure%20JMX.pdf

75. Zaghib K, Charest P, Dontigny M, Guerfi A, Lagace M, Mauger A, Kopec M, Julien CM (2010) $LiFePO_4$: from molten ingot to nanoparticles with high-rate performance in Li-ion batteries. J Power Sourc 195:8280–8288
76. Noh JK, Kim S, Kim H, Choi W, Chang W, Byun D, Cho BW, Chung KY (2014) Mechanochemical synthesis of Li_2MnO_3 shell/$LiMO_2$ (M = Ni, Co, Mn) core-structured nanocomposites for lithium-ion batteries. Sci Rep 4:4847
77. Zaghib K, Mauger A, Gendron F, Julien CM (2008) Surface effects on the physical and electrochemical properties of thin $LiFePO_4$ particles. Chem Mater 20:462–469
78. Zaghib K, Dontigny M, Charest P, Labrecque JF, Guerfi A, Kopec M, Mauger A, Gendron F, Julien CM (2008) Aging of $LiFePO_4$ upon exposure to H_2O. J Power Sourc 185:698–710
79. Axmann A, Stinner C, Wohlfahrt-Mehrens M, Mauger A, Gendron F, Julien CM (2009) Non-stoichiometric $LiFePO_4$: defects and related properties. Chem Mater 21:1636–1644
80. Julien CM, Mauger A, Zaghib K (2011) Surface effects on electrochemical properties of nano-sized $LiFePO_4$. J Mater Chem 21:9955–9968
81. Zhang X, Jiang WJ, Zhu XP, Mauger A, Lu D, Julien CM (2011) Aging of $LiNi_{1/3}Mn_{1/3}Co_{1/3}O_2$ cathode material upon exposure to H_2O. J Power Sourc 196:5102–5108
82. Hashem AMA, Abdel-Ghany AE, Eid AE, Trottier J, Zaghib K, Mauger A, Julien CM (2011) Study of the surface modification of $LiNi_{1/3}Co_{1/3}Mn_{1/3}O_2$ cathode material for lithium ion battery. J Power Sourc 196:8632–8637
83. Mauger A, Zaghib K, Groult H, Julien CM (2013) Surface and bulk properties of $LiFePO_4$: the magnetic analysis. ECS Trans 50–24:115–123
84. Aurbach D, Gamolsky K, Markovsky B, Salitra G, Gofer Y, Heider U, Oesten R, Schmidt M (2000) The stydy of surface phenomena related to electrochemical lithium intercalation into Li_xMO_y host materials (M = Ni, Mn). J Electrochem Soc 147:1322–1331
85. Yamada A, Koizumi H, Nishimura S, Sonoyama N, Kanno R, Yonemura M, Nakamura T, Kobayashi T (2006) Room-temperature miscibility gap in Li_xFePO_4. Nat Mater 5:357–360
86. Zhou F, Marianetti CA, Cococcioni M, Morgan D, Ceder G (2004) Phase separation in Li_xFePO_4 induced by correlation effects. Phys Rev B Condens Matter 69:201101
87. Gibot P, Casas-Cabanas M, Laffont L, Levasseur S, Carlac P, Hamelet S, Tarascon JM, Masquelier C (2008) Room-temperature single-phase Li insertion/extraction in nanoscale Li_xFePO_4. Nat Mater 7:741–747
88. Tang M, Huang HY, Meethong N, Kao YH, Carter WC, Chiang YM (2009) Model for the particle size, overpotential and strain dependence of phase transition pathways in storage electrodes: application to nanoscale olivines. Chem Mater 21:1557–1571
89. Zaghib K, Mauger A, Goodenough JB, Gendron F, Julien CM (2009) Positive electrode: lithium iron phosphate. In: Garche J, Dyer C, Moseley P, Ogumi Z, Rand D, Scrosati B (eds) Encyclopedia of electrochemical power sources, vol 5. Elsevier, Amsterdam, pp 264–296
90. Pandey NK, Tiwari K, Roy A (2011) Ag doped WO_3 nanomaterials as relative humidity sensor. Sensors J IEEE 11:2911–2918
91. Suisanti D, Diputra AA, Tananta L, Purwaningsih H, Kusuma GE, Wang C, Shih S, Huanf Y (2014) WO_3 nanomaterials synthesized via a sol-gel method and calcination for use as a CO gas sensor. Front Chem Sci Eng 8:179–187
92. Hoel A, Reyes LF, Heszler P, Lantto V, Granqvist CG (2004) Nanomaterials for environmental applicationq: novel WO_3-based gas sensors made by advanced gas deposition. Curr Appl Phys 4:547–553
93. Aliev AE, Park C (2000) Deveopment of WO_3 thin films using nanoscale silicon particles. Jpn J Appl Phys 39:3572–3578
94. Liang CC (1973) Conduction characteristics of the lithium iodide-aluminium oxide solid electrolytes. J Electrochem Soc 120:12891292
95. Wang Q, Wen Z, Jeong Y, Choi J, Lee K, Li J (2006) Li driven electrochemical properties of WO_3 nanorods. Nanotechnology 17:3116–3120
96. Wang J, Eugene Khoo E, Lee PS, Ma J (2008) Synthesis, assembly, and electrochromic properties of uniform crystalline WO_3 nanorods. J Phys Chem C 112:14306–14312

97. Yebka B, Pecquenar B, Julien C, Livage J (1997) Electrochemical Li^+ insertion in WO_3-xTiO_2 mixed oxides. Solid State Ionics 104:169–175
98. Pecquenard B, Lecacheux H, Livage J, Julien C (1998) Orthorhombic WO_3 formed via a Ti-stabilized $WO_3 \cdot 1/3H_2O$ phase. J Solid State Chem 135:159–168
99. Picquart M, Castro-Garcia S, Livage J, Julien C, Haro-Poniatowski E (2000) Sol-gel transition kinetics in WO_3 investigated by in-situ Raman spectroscopy. J Sol Gel Sci Technol 18:199–206
100. Ramana CV, Utsunomiya S, Ewing RC, Julien CM, Becker U (2005) Electron microscopy investigation of structural transformations in tungsten oxide (WO_3) thin films. Phys Status Sol A 202:R108–R110
101. Ramana CV, Utsunomiya S, Ewing RC, Julien CM, Becker U (2006) Structural stability and phase transitions in WO_3 thin films. J Phys Chem B 110:10430–10435
102. Yu DYW, Yanagida K (2011) Structural analysis of Li_2MnO_3 and related Li-Mn-O materials. J Electrochem Soc 158:A1015–A1022
103. Amalraj SF, Sharon D, Talianker M, Julien CM, Burlaka L, Lavi R, Zhecheva E, Markovsky B, Zinigrad E, Kovacheva D, Stoyanova R, Aurbach D (2013) Study of the nanosized Li_2MnO_3: electrochemical behaviour, structure, magnetic properties and vibrational modes. Electrochim Acta 97:259–270
104. Amdouni N, Zarrouk H, Soulette F, Julien C (2003) $LiAl_yCo_{1-y}O_2$ ($0.0 \leq y \leq 0.3$) intercalation compounds synthesized from the citrate precursors. Mater Chem Phys 80:205–214
105. Amdouni N, Zarrouk H, Julien CM (2003) Structural and electrochemical properties of $LiCoO_2$ and $LiAl_yCo_{1-y}O_2$ ($y = 0.1$ and 0.2) oxides. A comparative study of electrodes prepared by the citrate precursor route. Ionics 9:47–55
106. Minakshi M, Blackford M, Ionescu M (2011) Characterization of alkaline-earth oxide additions to the MnO_2 cathode in an aqueous secondary battery. J Alloys Compd 509:5974–5980
107. Park DH, Ha HW, Lee SH, Choy JH, Hwang SJ (2008) Transformation from microcrystalline $LiMn_{1-x}Cr_xO_2$ to 1D nanostructured β-$Mn_{1-x}Cr_xO_2$: promising electrode performance of β-MnO_2-type nanowires. J Phys Chem C 112:5160–5164
108. Abuzeid HM, Hashem AM, Narayanan N, Ehrenberg H, Julien CM (2011) Nanosized silver-coated and doped manganese dioxide for rechargeable lithium batteries. Solid State Ionics 182:108–115
109. Hashem AM, Groult H, Mauger A, Zaghib K, Julien CM (2012) Electrochemical properties of nanofibers α-MoO_3 as cathode materials for Li batteries. J Power Sourc 219:126–132